Electrolyte Motion Induced Salt Inhomogeneity – A Novel Aging Mechanism in Large-Format Lithium-Ion Cells

Sophie Solchenbach[a,#], Camilla Tacconis[a], Aurora Gomez Martin[a], Verena Peters[a], Lea Wallisch[a], Anna Stanke[a], Johanna Hofer[a], Diemo Renz[a], Burkhard Lewerich[a], Georg Bauer[a], Moritz Wichmann[a], Daniel Goldbach[a], Alexander Adam[a], Markus Spielbauer[a], Peter Lamp[a], Johannes Wandt[a,b,#]

[a]BMW AG, 80788 Munich, Germany

[b]University of Agder, 4869 Grimstad, Norway

#corresponding authors: sophie.solchenbach@bmw.de, johannes.wandt@bmw.de

Abstract

The electrification of the transport sector places ever-increasing demands on the energy density, fast-charging performance, and lifetime of lithium-ion cells. In this study, we investigate fast-charging of high energy density (~ 800 Wh/L) prototype cylindrical 4695 lithium-ion cells with two different ("low" and "high") electrolyte amounts. Using pore volume calculations, computer tomography and moment of inertia measurements, we find that the volume change of the active material causes electrolyte motion into and out of the jelly roll upon cycling in the high electrolyte cells, while no electrolyte motion occurs in the low electrolyte cells. At the same time, the high electrolyte cells show a significantly worse capacity retention during fast charge cycling compared to the low electrolyte cells (24% vs. 5% capacity loss after 130 cycles). We demonstrate that a coupling of in-plane electrolyte motion with the through-plane $LiPF_6$ concentration gradient rapidly causes a strong $LiPF_6$ concentration gradient along the jelly roll height (= in-plane) on a cm-scale: After only 18 cycles, $LiPF_6$ concentrations at the jelly roll edges and center (as determined by ion-chromatography) deviate by more than ± 50% in comparison to the initial average value. We term this hitherto unknown effect *"electrolyte motion induced salt inhomogeneity"* (EMSI). This long-scale salt concentration gradient causes a loss of cell capacity, an increase in resistance, and eventually highly localized lithium plating. Finally, we discuss the far-reaching implications of the EMSI effect on cell design and testing, not only for cylindrical cells but any large-format lithium-ion cell under high compression.

Graphical Abstract

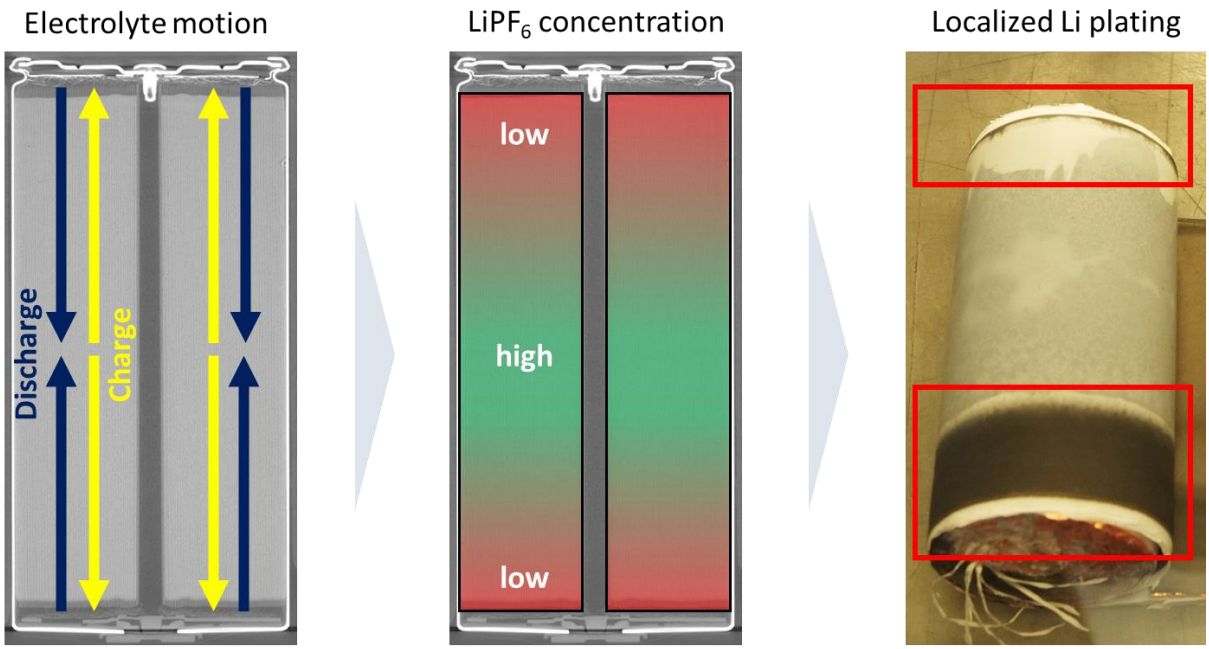

Introduction

As the electrification of the transport sector advances, the energy density of lithium-ion cells continuously increases. On the material level, this is achieved by using active materials with higher lithiation capacities, like silicon or Ni-rich layered oxide materials; on the electrode level, the active material mass loading (in mg/cm^2) is increased along with reducing the electrode porosity.[1,2] At the same time, ever shorter fast charge times are desirable to reduce the overall travel time during long-distance trips with an electric vehicle. The fast charge capability of a lithium-ion cell is usually limited by the onset of lithium plating, which occurs when the negative electrode surface potential decreases below 0 V vs. Li/Li$^+$. For a given cell chemistry (active materials and electrolyte formulation) and charging condition (C-rate and temperature), this lithium plating onset depends primarily on active material loading and electrode porosity, thus creating a direct conflict of interest between fast charging capability and energy density.[2]

While active material loading and electrode porosity should be very homogenous across electrodes in commercial large-format cells, there are numerous reports of highly inhomogeneous lithium plating patterns in cycled prismatic[3–5] and cylindrical cells,[6,7] which is typically assigned to macro-scale inhomogeneities in temperature, pressure, or material loading.[8–11] In 18650 cells, a common pattern are horizontal lithium plating stripes which run along the upper and lower end of the anode.[7] As discussed in detail below, these lithium plating stripes are of special interest to us as we have made similar observations in different cylindrical cell formats. Another interesting observation is the highly localized lithium plating reported by Smith et al.[5] in a 48 Ah prismatic cell after cycling at 23 °C with a charging rate of C/2, while using steel plates for cell compression. At such a low charging rate, electrode kinetics and lithium transport should be fast enough to prevent "classical" lithium plating; therefore, the authors suggested a novel deactivation mechanism based on high local stress.

Besides inhomogeneous lithium plating, there is another peculiar behavior which – to the best of our knowledge – only occurs in large-format lithium-ion cells, namely the so-called *"capacity recovery"*. Both cylindrical and prismatic cells have been reported to recover significant fractions of an apparent rapid capacity loss if the cells were rested for weeks to months after cycling.[12–15] The recovered capacities range from ≈8 to ≈30% of total cell capacity (i.e., beyond what can be explained by the well-known anode overhang lithiation/delithiation[13,16]) and are typically accompanied by a significant decrease in cell resistance. The recovery effect strongly depends on the depths of discharge[13,14] and increases with higher C-rates during cycling.[14,15] Furthermore, a recent study of Bonakdarpour et al.[15] shows that capacity loss and resistance growth, as well as the subsequent capacity recovery during rest, *increase* in 18650 cylindrical cells when the electrolyte amount is increased. This positive correlation of cell aging and electrolyte amount, which the authors call *"high volume effect"*, is somewhat unexpected as higher amounts of electrolyte are typically associated with better lifetime performance.[17,18] Finally, another unexpected effect is the influence of cell orientation and gravitation

on the aging behavior of 18650 cells, which the authors assign to an inhomogeneous distribution of liquid electrolyte within the jelly roll.[17]

Over the last few years, we have observed all the above-described behaviors in large-scale lithium-ion cells, namely i) highly localized lithium plating (even at low charging C-rates), ii) significant capacity recovery, iii) the adverse effect of high electrolyte amounts, and iv) the influence of cell orientation on the aging behavior. Of course, we cannot properly assess the respective origins of these effects for the different studies cited above, but we hypothesize that all these effects observed in our large-format cells might be caused by one single failure mechanism which is fundamentally triggered by electrolyte motion. Electrolyte motion has been observed indirectly by neutron radiography via rising and falling levels of free electrolyte outside the jelly roll more than 20 years ago for prismatic cells[18] and more recently also for cylindrical cells[19,20] but has not attracted wide-spread attention (as it should have) in the battery community. Finally, in 2023 a seminal publication by Dahn and co-workers[21] recognized electrolyte motion as an important aspect in and of itself.

In the present study, we investigate 4695 cylindrical cells produced on a BMW internal prototype line containing two different electrolyte amounts ("high" or "low"). First, we use theoretical calculations, computer tomography imaging, and moment of inertia measurements to show that the electrolyte amount determines whether electrolyte motion occurs (or whether it does not) in a lithium-ion cell. Next, the lifetime behavior of these cells during fast charge is investigated. Spatially resolved *post-mortem* analysis reveals that electrolyte motion causes an in-plane salt concentration gradient in the electrolyte along the axial direction of the jelly roll. We suggest a mechanism for how exactly electrolyte motion leads to this in-plane salt gradient; then, electrochemical simulations are applied to demonstrate that this in-plane salt gradient causes localized lithium plating upon fast-charging. Finally, we discuss the far-reaching implications of this in-plane salt gradient on various aspects of lithium-ion cell design and testing.

Results and discussion

4695 cylindrical cells

Throughout this study, we used cylindrical lithium-ion cells with a diameter of 46 mm and a height of 95 mm, a format which is called "4695" according to common battery cell convention. These specific cells were produced at a BMW-internal prototype line for research and development purposes and are not used in any vehicle project. The cells were designed as high energy density cells with a specific energy of ~ 300 Wh/kg_{cell} and a volumetric energy density of ~ 800 Wh/L_{cell}. Due to confidentiality reasons, we cannot disclose all design parameters in full detail; where this is the case, we state approximate values (indicated by a ~ symbol), ranges or use normalization.

The cell can consisted of steel with a wall thickness of ~ 500 µm; the jelly roll was connected to the cell can by a "tabless" design (also called "continuous tabbing") similar but not fully identical to the description in reference [22]. The anode active material was comprised of a mixture of graphite and a low amount of silicon (< 10 weight-%); as cathode active material, a layered nickel manganese cobalt oxide (NMC) with a high nickel content (> 85 atomic-%) was used. Within the full-cell cut-off voltages of 2.8 and 4.2 V, the cathode had a reversible areal capacity of ~ 4 mAh/cm^2; the anode areal capacity exceeded the cathode by ~5%, resulting in a N/P-ratio of ~1.05. A state-of-the art electrolyte was used consisting of linear and cyclic carbonates as solvents, fluoroethylene carbonate (FEC) as solid-electrolyte interphase (SEI) forming additive and 1.2 mol/L $LiPF_6$ as conducting salt. During cell formation (e.g. first charging), gaseous reaction products were removed from the jelly roll and cell by applying under pressure before finally sealing the cell.

Two sets of cells (see Table 1) were prepared which only differed in the amount of electrolyte, namely < 1.30 and 1.45-1.50 $g_{electrolyte}/Ah_{cell}$. These cells are denoted as "low" and "high" electrolyte cells within this study, but we want to remind the reader that both electrolyte amounts are very low in comparison to what is typically used in academic and industrial lithium-ion cells ("low" and "very low electrolyte cells" might have been more suitable labels).[23,24] The low electrolyte cells have a slightly lower capacity (-1.2%) and a higher pulse resistance (+ 8.6%) in comparison to the high electrolyte cells (rows 2 and 3 in Table 1). The low standard deviations for cell capacity and pulse resistance indicate a very low cell to cell variation for the prototype cells used in this study.

Table 1 Electrolyte amount, normalized C/3 capacity and normalized direct current internal resistance (DCIR) for high and low electrolyte cells. Capacity and DCIR values were normalized to the average of the high electrolyte cells. The error represents standard deviations for around 12 cells each.

	High electrolyte cells	Low electrolyte cells
Electrolyte filling amount	1.45-1.50 g/Ah	< 1.3 g/Ah
Capacity (C/3 discharge, 25 °C)	100 ± 0.2%	98.8 ± 0.5%
DCIR (30 s, 2C, 50% SOC, 25 °C)	100 ± 1.7%	108.6 ± 2.1%

Pore filling ratio and electrolyte motion

The fundamental reason for electrolyte motion in lithium-ion cells is the reversible volume change of the active materials in a constrained cell housing. Figure 1a shows the change in unit cell volume of graphite, NMC, and silicon as a function of their states of lithiation (SOL). During lithium intercalation (C_6 to LiC_6), graphite expands by 13%; the graphite volume change is non-linear and takes place mostly in the early diluted stages ($0 < SOL < 0.25$) and during the stage 2 – stage 1 transition ($0.5 < SOL < 1.0$), corresponding to an average volume increase of 4.2 mL/mol of lithium.[25,26] Silicon, which is not an intercalation but an alloying anode material, expands linearly by 280% upon full lithiation (Si to $Li_{3.75}Si$) due to a constant volume requirement of 8.9 mL/mol of lithium.[26,27] The nickel-rich NMC cathode material contracts during delithiation ($Li_{1.0}MO_2$ to $Li_{0.2}MO_2$ where M is the transition metal) by 5%, with most volume change taking place during the H2 – H3 transition ($SOL < 0.3$).[28,29]

Figure 1b shows how the SOL of the different active materials correlates with the state of charge (SOC) in our 4695 cells. As NMC is the only cathode active material, its SOL shows a linear correlation with the cell SOC. On the anode side, graphite is electrochemically active mostly at high and silicon mostly at low SOCs due the different open-circuit voltage (OCV) potentials of the two materials.[30,31] Combining the known masses and densities of the pristine active materials with the SOL dependent volume expansion (Figure 1a) and the SOL-SOC correlation (Figure 1b) allows us to calculate the SOC-dependent active material volume $V_{\mathrm{ActiveMaterial}}$, which equals ≈ 73 mL and ≈ 78 mL at 0% and 100% SOC, respectively (Figure 1c, green area). The change of $V_{\mathrm{ActiveMaterial}}$ can be divided into three distinctive regions, namely i) a region of strong volume increase at low SOCs up to 30% SOC when both silicon is active (Figure 1b) and graphite is in the diluted lithiation states ($SOL < 0.25$, Figure 1a), then ii) an intermediary region between 30% and 60% SOC with a close to constant value for $V_{\mathrm{ActiveMaterial}}$ and iii) a region with moderate volume increase, in which graphite undergoes the stage 1 – stage 2 transition, but the associated expansion is partially counteracted by the NMC contraction (see Figure 1a).

In addition to the active material, the jelly roll also contains aluminum and copper current collector foils, separator, polymer binders, and conductive additives as inactive materials. The volume of these inactive materials $V_{\mathrm{InactiveMaterial}}$ is SOC-independent and equals ≈ 22 mL (see grey area in Figure 1c). Note that this volume also includes ≈ 2 mL of solid electrolyte interphase (SEI) volume, which we estimate using a simple model for FEC reduction (see Supporting Information for further information).

Now that we have identified the volume of all solid materials inside the jelly roll (sum of $V_{\mathrm{ActiveMaterial}}$ and $V_{\mathrm{InactiveMaterial}}$), we can compare this to the entire jelly roll volume $V_{\mathrm{JellyRoll}}$, which can be directly determined by X-ray computer tomography (CT). For our 4695 cells, $V_{\mathrm{JellyRoll}}$ equals ≈ 135 and ≈ 136 mL (excluding the hollow core in the center) at 0% and 100% SOC as indicated in Figure 1c by the black line. The jelly roll volumes are very similar at 0% and 100% SOC as the circular cell housing exerts high counter-pressure and prevents significant jelly roll expansion (the jelly roll is already in close contact with the cell can at 0% SOC). According to

$$V_{Pore}(SOC) = V_{JellyRoll} - V_{ActiveMaterial}(SOC) - V_{InactiveMaterial} \quad (1)$$

we can determine the SOC-dependent pore volume V_{Pore}, yielding ≈ 40 mL and ≈ 35 mL at 0 and 100% SOC, respectively (Figure 1c, blue area). Note that these pore volumes include the porosities in the anode, cathode, and separator. As cell swelling is suppressed due to the rigidity of the circular can, the only accessible void volume to accommodate the increase in $V_{ActiveMaterial}$ is the pore volume within the electrodes and potentially the separator. Therefore, the SOC-dependencies of $V_{ActiveMaterial}$ and V_{Pore} are exactly opposite.

Finally, we can compare V_{Pore} to the electrolyte volume $V_{Electrolyte}$ which is present in the beginning-of-life (BOL) cell after formation. Based on our FEC reduction model, $V_{Electrolyte}$ is 5-6% smaller than the volume which had been filled into the cell during cell assembly due to electrolyte loss during initial SEI formation (see Supporting Information for further details). In this respect, the pore filling ratio *PFR*, defined as

$$PFR(SOC) = \frac{V_{Electrolyte}}{V_{Pores}(SOC)} \quad (2)$$

is a very useful parameter. For the high electrolyte cells (red line in Figure 1d), the pore filling ratio exceeds 1.00 at SOCs ≥ 20%, meaning that the electrolyte volume exceeds the shrinking total pore volume inside the jelly roll. Upon charging beyond 20% SOC, electrolyte has to be expelled out of the jelly roll - similar to squeezing water out of an already fully wetted sponge -, thus giving rise to electrolyte motion. At a SOC of 100%, a pore filling ratio of 1.08 corresponds to the generation of ≈ 3 mL of free electrolyte outside the jelly roll for the high electrolyte cells. During subsequent discharging the process is reversed, and electrolyte flows back into the jelly roll.

In contrast, the low electrolyte cells show a pore filling ratio *PFR* below 1.00 at all SOCs, meaning that no free electrolyte will be generated because the jelly roll can always accommodate all electrolyte. Therefore, we expect no electrolyte motion to occur in the low electrolyte cells, as the jelly roll behaves like a non-fully wetted sponge which can be squeezed a little without water dripping out. Considering the low pore filling ratio of ≈ 80% at 0% SOC (= end of discharge when the cell capacity is determined), it is quite astonishing that the low electrolyte cells only have 1% less cell capacity than the high electrolyte cells (see Table 1). This is an indication for a homogeneous electrolyte distribution throughout the entire jelly roll, meaning that all pores are close to the average pore filling ratio, rather than some regions with full and other regions with little or no wetting.

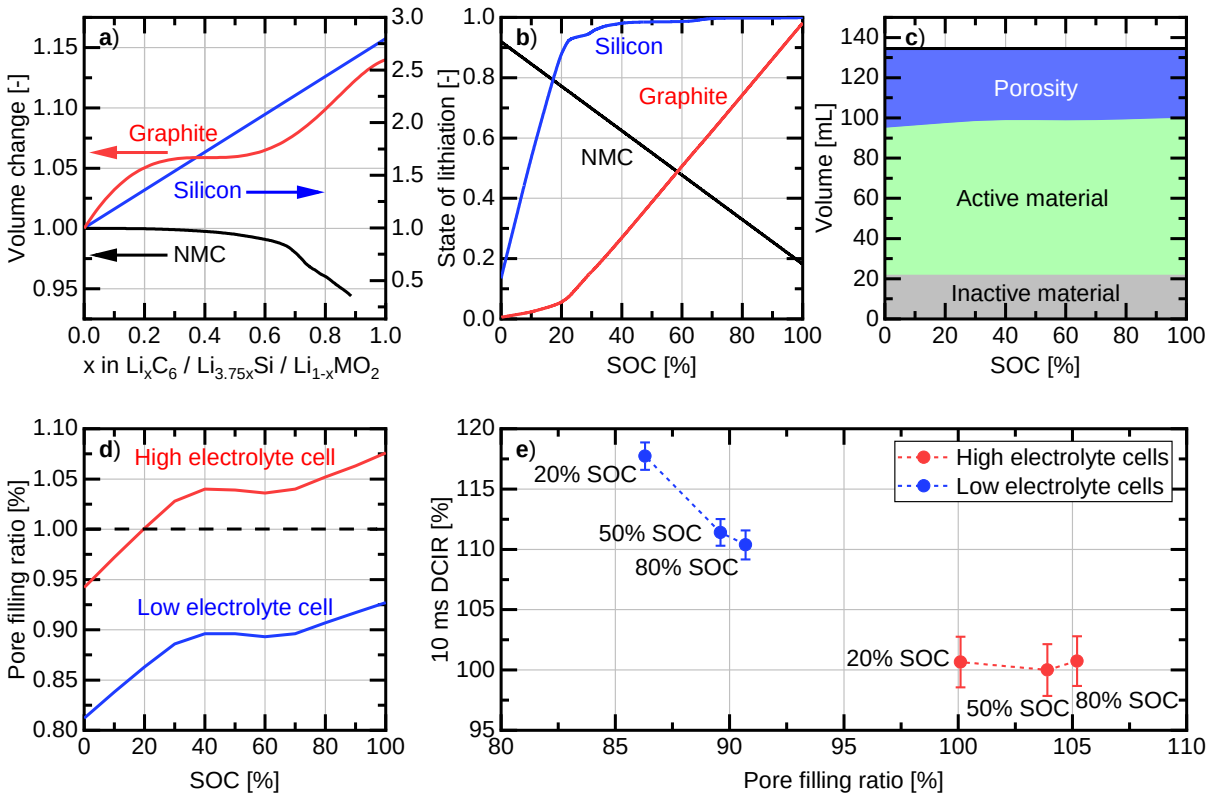

Figure 1 a) Unit volume cell expansion for graphite, NMC and silicon as a function of state of lithiation (SOL); b) state of lithiation of active materials as function of cell SOC in the 4695 cells; c) volume of active material $V_{\text{ActiveMaterial}}$ (sum of NMC, graphite and silicon), inactive material $V_{\text{InactiveMaterial}}$ and pore volume V_{Pore} as a function of SOC in the 4695 cells; d) pore filling ratio as function of SOC for high and low electrolyte 4695 cells; e) 10 ms pulse resistance at 20%, 50% and 80% SOC for high and low electrolyte cells normalized to the 10 ms pulse resistance of the high electrolyte cells at 50% SOC. Note that in Figure 1a, the state of lithiation of Si refers to the theoretical specific capacity $Q_{\text{theo.}}$(Si) of 3590 mAh/g, whereas it refers to the lower practical specific capacity Q_{real}(Si) in Figure 1b (see Methods section for further details).

In essence, the SOC-dependent pore filling ratio *PFR* can be a useful design parameter that helps to differentiate whether a cell is expected to exhibit electrolyte motion (*PFR* > 1) or not (*PFR* < 1 at all SOCs). We want to stress that a *PFR* value >> 1.00 (as in our high electrolyte cells) is currently state-of-the art in commercial cells,[23] while our low electrolyte cells with a *PFR* < 1 would rather be considered as an oddity. Unfortunately, it is quite challenging to calculate the *PFR* with sufficient precision (± 0.05) for a proper assessment of whether electrolyte motion is expected to occur, but pulse resistance data turns out to be helpful to substantiate our *PFR* estimation. Figure 1e shows the 10 ms pulse resistance for the low and high electrolyte cells normalized to the 10 ms resistance of the high electrolyte cell at 50% SOC as a function of the calculated pore filling ratio. For the high electrolyte cells (complete pore filling at all sampled SOCs, see Figure 1d), the 10 ms resistance is SOC-independent within the error bars. The 10 ms resistance of the low electrolyte cells differs in two ways as it i) is significantly higher than that of the high electrolyte cells and ii) shows a clear downward trend with increasing SOC. A likely explanation is that the low electrolyte cell exhibits a higher ionic resistance within the separator and electrodes due to incomplete pore filling.[32,33] With increasing SOC,

the pore filling ratio of the low electrolyte increases (see Figure 1d), which would then also cause the 10 ms resistance to decrease, as experimentally observed. According to this interpretation, the characteristic SOC-dependency of the 10 ms cell resistance supports our pore filling ratio calculation, namely *PFR* values of > 1.0 for the high electrolyte and < 1.0 for the low electrolyte cells. In the next section, we will present further evidence for the occurrence of electrolyte motion in the high electrolyte cell and its absence in the low electrolyte cell.

Assessment of electrolyte motion by computer tomography

The "free" electrolyte outside of the jelly roll can be located in the hollow core in the center of the jelly roll (blue shaded area in Figure 2c), and/or in the region directly above and below the jelly roll, which we call "donut region" as it resembles the upper and lower part of a horizontally cut donut (red shaded areas in Figure 2c). The donut region is comprised of the separator extending beyond the electrodes and bare, un-coated current collector foils (aluminum foils on upper side, copper foils on lower side) which electronically connect the jelly roll to the cell housing. In between the current collector foils, there is a total void volume of ≈ 8.5 mL in the donut region (top and bottom combined) which compares to only ≈ 1.5 mL of void volume inside the hollow core. From a quick glance at Figure 2c, it might be counterintuitive that the void volume in the donut region is significantly larger than the hollow core, but this simply reflects the more pronounced influence of diameter d ($V \propto d^2$) over height h ($V \propto h$) for the volume V of a cylinder. Note that the void volume ratio of core and donut region differs significantly for different cylindrical cell formats, e.g., in an 18650 cell, the core would have a much larger share of total void volume compared to a 4695 cell.

As a next step, we considered computer tomography (CT) images for the presence/absence of free electrolyte as a function of SOC in the 4695 cells. Figure 2a and b show horizontal cross sections through the donut region just below the lower end of the jelly roll (see dashed yellow line in Figure 2c) for a low electrolyte cell at 0% and 100% SOC. Both images look very similar and free electrolyte is visible in neither of them, as expected based on the calculated *PFR* < 1 over the entire SOC range (see Figure 1d). For the high electrolyte cell, no free electrolyte is visible at 0% SOC (Figure 2d); however, at 100% SOC (Figure 2e) free electrolyte is visible as darker patches of concentric shape. Based on the share of area covered by electrolyte and the total donut region void volume of ≈ 8.5 mL, we estimate the volume of free electrolyte to be roughly 2 to 3 mL at 100% SOC and 0 mL at 0% SOC for the high electrolyte cell. These values match well with our pore filling calculation for the high electrolyte cell (0 and ≈ 3 mL of free electrolyte at 0% and 100% SOC, respectively).

To assess if free electrolyte is also present in the hollow core, Figure 2f shows an additional vertical cross section CT image of a high electrolyte cell at 100% SOC zoomed in on the lower part of the core, where free electrolyte would be expected to accumulate due to gravity as the CTs scan was measured with the cell in upright position. Note that in Figure 2f (and also in Figure 2c), the grey scale is inverted in comparison to Figure 2a-b and d-e, so that regions of high density are now displayed in bright color

(e.g., the steel-housing), whereas regions of low density are displayed in dark color (e.g., most of the hollow core). Upon close inspection, some additional free electrolyte is visible in Figure 2f in the lower right side of the core as a bright grey shade; this free electrolyte is probably adhering to the separator which is wrapping the inner side of the jelly roll. However, the vast majority of the core in Figure 2f appears empty, indicating that most of the free electrolyte at 100% SOC is present in the donut region and not in the hollow core. In summary, computer tomography suggests that 2 to 3 mL of electrolyte move out of the jelly roll upon charging in the high electrolyte cell while no electrolyte motion is discernable for the low electrolyte cell.

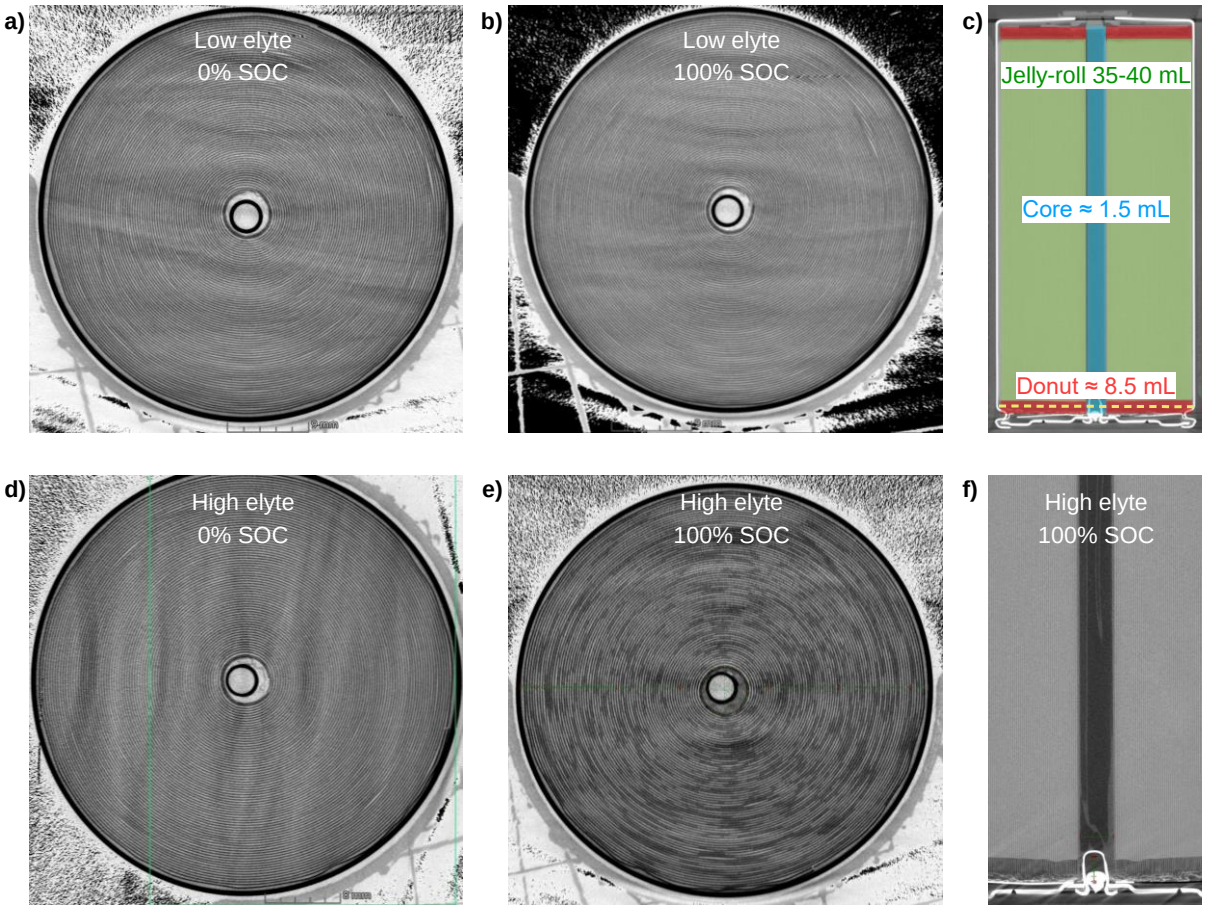

Figure 2 CT-images of low electrolyte and high electrolyte 4695 cells. a and b) Horizontal cross sections through lower donut region of a low electrolyte cell at 0% and 100% SOC; in both images, no free electrolyte is visible. c) Vertical cross section with schematic subdivision into jelly roll (green area, 35-40 mL pore volume), hollow core in the center (blue area, ≈ 1.5 mL void volume) and donut regions above and below jell-roll (red area, ≈ 8.5 mL void volume); the yellow dashed line indicates the position of the horizontal cross sections shown in panels a-b and d-e. d) and e) Horizontal cross sections through lower donut region of a high electrolyte cell at 0% and 100% SOC, where free electrolyte is visible at 100% SOC as dark concentric patches. f) Vertical cross section through the lower part of a high electrolyte cell with a zoom on the hollow core. Note that the greyscale is opposite in panels a-b and d-e (bright = low material density) in comparison to panels c and f (bright = low material density).

Assessment of electrolyte motion by moment of inertia change

A elegant way to track electrolyte motion in cylindrical cells is to measure the change of the moment of inertia upon charging and discharging, as recently published by Aiken *et al*.[21] The basic idea is simple: when electrolyte is pressed out of the jelly roll into the donut region, mass is moved from the central part of the cell towards its terminal sides. This causes an increase in moment of inertia around a rotation axis which is perpendicular to the long axis of the cylindrical cell (see Figure 3a). Rearranging equation 1 from ref. [21] gives

$$m_2 = \frac{1}{2}\left(\frac{I_{\mathrm{SOC\ 100\%}}}{I_{\mathrm{SOC\ 0\%}}} - 1\right) \cdot m_1 \tag{3}$$

where m_2 is the mass of electrolyte moved from the jelly roll into the donut region (blue area in Figure 3b), $I_{\mathrm{SOC\ 100\%}}$ and $I_{\mathrm{SOC\ 0\%}}$ are the moments of inertia at 100 and 0% SOC, respectively, and m_1 is the cell mass (red area in Figure 3a). Equation 3 (and the original equation 1 in ref. [21]) is derived from the moment of inertia of a thin rod which assumes that the radius is significantly lower than its length. This is still an acceptable approximation for the 4695 cell format as the length of the cell is ≈ 4x larger than the radius. Note that equation 3 holds true only as long as electrolyte moves from the jelly roll into the donut region. Once free electrolyte starts to "overflow" into the hollow core, the correlation between electrolyte motion and moment of inertia change becomes much more complex without a unique solution of electrolyte distribution for a given $I_{\mathrm{SOC\ 100\%}}/I_{\mathrm{SOC\ 0\%}}$ value, as discussed in detail by Aiken *et al*.[21] Fortunately, the CT-images (Figure 2) suggest that free electrolyte is mostly present in the donut region in the high electrolyte cell used within this study.

Figure 3c-e show the moment of inertia normalized to the average of the initial two $I_{\mathrm{SOC\ 0\%}}$ values at 0% and 100% SOC for the low and high electrolyte cells as a function of time. In each panel, the time $t = 0$ corresponds to the first of several consecutive moment of inertia measurements, recorded approximately 5 to 15 minutes after termination of the previous C/15 discharge (Figure 3c and e) or charge (Figure 3d), respectively. Charging and discharging are carried out at a rate of C/15 to prevent any thermal expansion or build-up of concentration gradients. For the high electrolyte cells, the moment of inertia increases by ≈ 1.3% between 0% and 100% SOC. According to equation 3 and the cell of mass of 400-450 g, this corresponds to the movement of ≈ 3 g or ≈ 2.4 mL of electrolyte from the jelly roll into the donut volume for the high electrolyte cells. As expected, the moment of inertia change is significantly smaller for the low electrolyte cells, but it also clearly does not equal zero. A possible interpretation is the occurrence of a minor jelly roll internal electrolyte redistribution as discussed in detail in the Supporting Information. In both the high and low electrolyte cells, the moment of inertia returns to the initial value when discharged back to 0% SOC (Figure 3e), indicating that the electrolyte motion is fully reversible at least for the low C/15 rate applied here. Furthermore, for this low C-rate and our time resolution (order of magnitude of several minutes) the moment of inertia hardly changes during OCV which is markedly

different from the highly dynamic behavior observed by Aiken *et al*. in their *operando* experiments (= very high time resolution) and higher cycling C-rates.

In summary, moment of inertia measurements, pore volume calculations and CT images all suggest that electrolyte motion occurs in the high electrolyte cells, while little or no electrolyte motion takes place in the low electrolyte cells. In the next sections we will investigate the impact of electrolyte motion on the aging behavior during cell cycling.

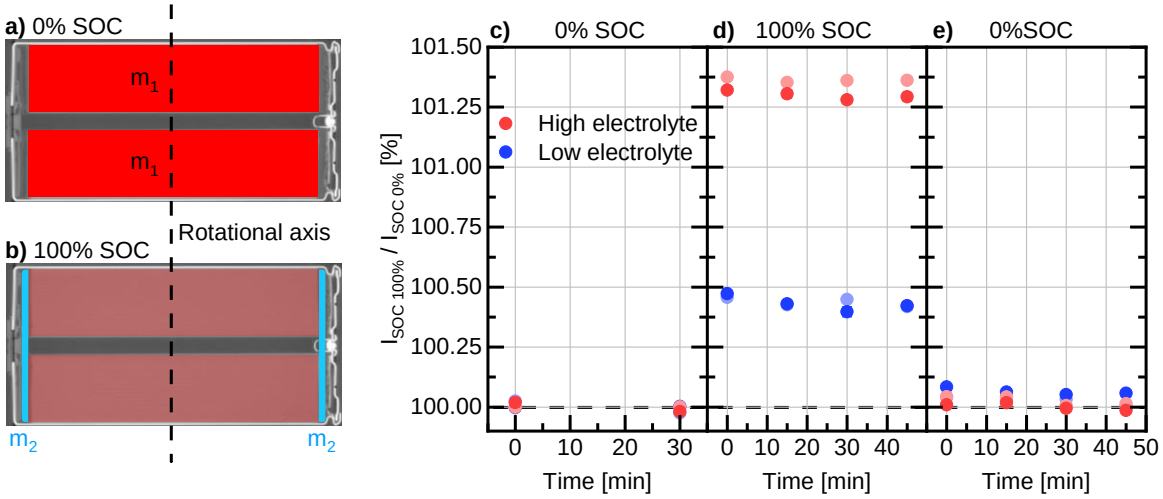

Figure 3 Moment of inertia change of 4695 cells upon charging and discharging; a) and b) schematics of electrolyte location in a cylindrical cell at low SOC (all electrolyte in jelly roll, m_1 is total cell weight) and at high SOC (electrolyte of mass m_2 moved into donut region), the black vertical dashed line symbolizes the rotation axis perpendicular to which the electrolyte motion affects the moment of inertia; c-e) moment of inertia change between 0 and 100% SOC for the high and low electrolyte 4695 cells normalized to the initial SOC 0% value, measured with the cell oriented horizontally as displayed in panels a and b; the dark and bright blue and red dots represent two individual measurement series for low and high electrolyte cells; note that each data point contains error bars which indicate the standard deviation of 3 repeated measurements; the error bars are hardly visible due to very high precision of our experimental set-up.

Influence of electrolyte volume and cell orientation on fast charge cycling behavior

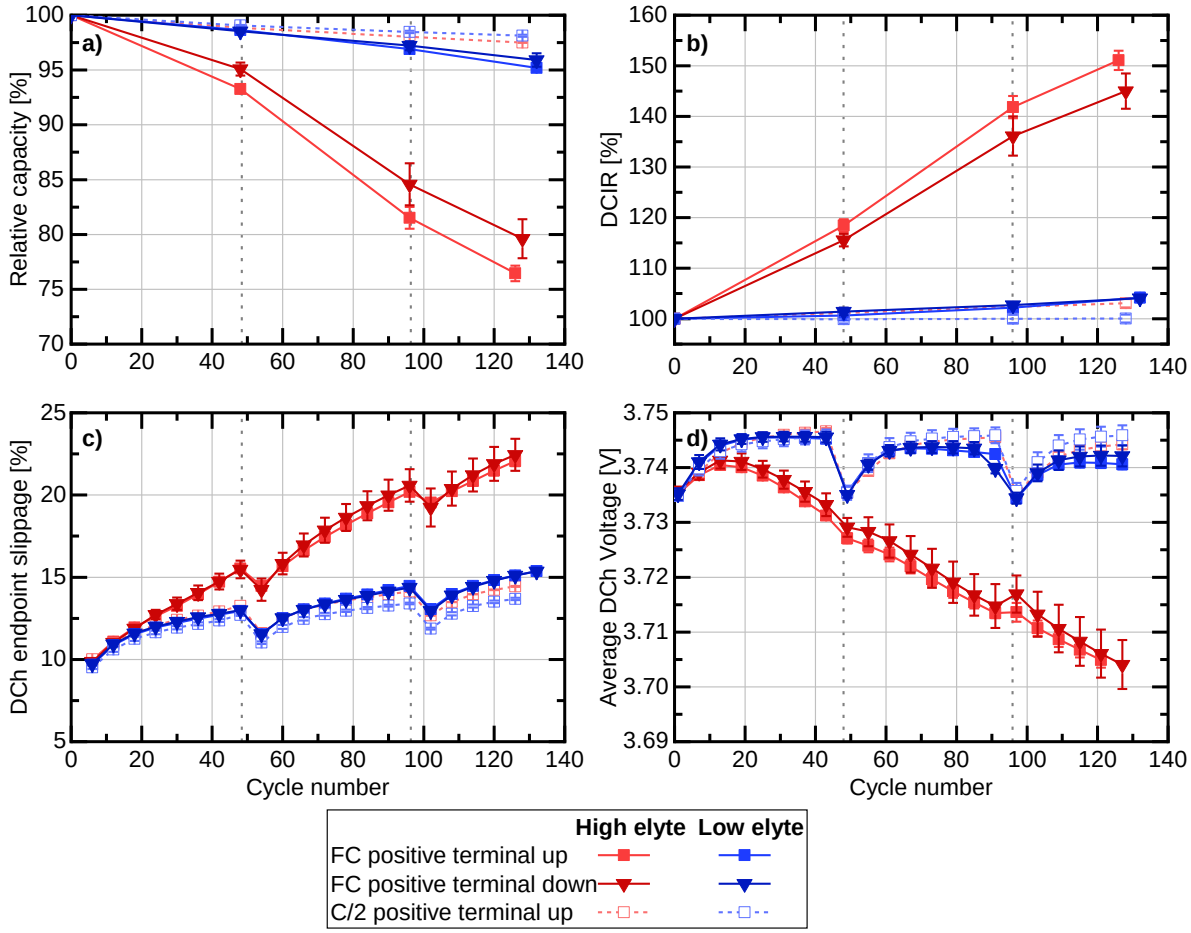

Figure 4 Cycling test with high electrolyte (red) and low electrolyte (blue) cells with either i) 16 – 21 min fast charging protocol for two vertical orientations (positive terminal up = closed squares, positive terminal down = closed triangles) or ii) C/2 charging (positive terminal up, open squares) as reference. Reference performance tests (RPT), carried out after each 48 aging cycles at 25 °C: a) relative C/3 discharge capacity and b) relative direct current internal resistance (DCIR, 30 s 2C discharge pulse at 50% SOC). Aging cycling at 35 °C: c) discharge endpoint slippage (normalized to initial cell capacity) after every 6th cycle (i.e., after each 3x C/2/C/2 + 3x FC/C/2 sequence) and d) average discharge voltage (= energy / capacity from CC discharge) during the first C/2 cycle of each 3x C/2/C/2 + 3x FC/C/2 sequence. Error bars indicate min/max values from two reproduced cells.

High and low electrolyte cells were cycled at 35 °C with a multi-step constant current fast charge current profile (see Figure S3) from 10 to 80% SOC with a charging time of 16 - 21 min (exact charging time cannot be disclosed). The fast charge cycling consisted of a repeating sequence of three consecutive fast charging (FC) and three consecutive C/2 charging cycles (= 3x C/2/C/2 + 3x FC/C/2), so 50% of all charges were fast charge. This cycling protocol was applied to high and low electrolyte cells with the positive terminal facing upwards during cycling (red and blue closed squares in Figure 4) and cells with the positive terminal facing downwards (red and blue closed triangles in Figure 4). In addition, high and low electrolyte cells were also subjected to a cycling procedure in which all cycles were carried out with a C/2 charging rate (= 3x C/2/C/2 + 3x C/2/C/2), but only with the positive terminal facing upwards (red and blue open squares in Figure 4). After every 48 cycles (= 8 repetitions of the sequence of 6 cycles) a

reference performance test (RPT) was carried out for all cells to determine the C/3 CC discharge capacity and direct current internal resistance (DCIR) at 25 °C. Further details on the cycling protocol are given in Table 2 (Methods section).

Figure 4a and b show capacity and DCIR evolution as measured during RPTs. The high electrolyte fast charge cells cycled with the positive terminal facing up (red closed squares) showed a strong capacity fade of 24% within ≈130 cycles (Figure 4a), while the high electrolyte C/2 cells cycled in the same orientation but without fast charge (red open squares) only show a capacity loss of 2.5%. The high electrolyte fast charge cells cycled with the positive terminal facing down (red closed triangles) also show a strong capacity fade of 20%, albeit somewhat less severe than their counterparts with the positive terminal facing up (red closed squares). The difference between cycling conditions is significantly lower for the low electrolyte cells: Here, both the fast charge cells with the positive terminal facing up (blue closed squares) and down (blue closed triangles) show a remaining capacity of 95%, i.e., only 3% less capacity compared to the C/2 cells (98% capacity after 130 cycles, blue open squares). The same overall trend is also visible in the cell resistance (see Figure 4b), where the high electrolyte fast charge cells cycled with the positive terminal facing up (red closed squares) and down (red closed triangles) show a resistance increase of 50% and 45%, respectively, while the resistance for the low electrolyte fast charge cells in both orientations only increases about 5% (blue closed squares and triangles). Interestingly, the high electrolyte C/2 cells show a resistance increase of 3% after 130 cycles (red open squares), while for the low electrolyte C/2 cells (blue open squares), no resistance increase was measured, although the low electrolyte cells show an overall higher initial resistance (see Figure 1e).

To gain further insight into the evolution of the aging behavior, we also assessed the aging cycles in between the RPTs (Figure 4c and d). Figure 4c shows the discharge endpoint slippage (DEP) after each 6^{th} cycle (i.e., after each 3x C/2/C/2 + 3x FC/C/2 sequence) normalized by the initial cell capacity. The DEP is typically considered to be an indicator for side reactions occurring at the anode involving loss of cyclable lithium.[34] As the lower SOC is 10% during aging cycling (see Table 2 in Methods Section for details), all cells start with a DEP of 10%. For the first 18 cycles, the DEP of all cells shows a similar upwards trend, most likely due to continuous SEI formation, which is more pronounced during early cycles, or the (reversible) trapping of lithium in the crystalline silicon phase (see below). After cycle 18, the DEP of the high electrolyte fast charge cells (red closed squares and triangles) continues to shift upwards at an almost identical rate, leading to a significantly higher discharge endpoint slippage compared to the high electrolyte C/2 cells (red open squares, 22% vs. 14% after 130 cycles). Hence, the strong capacity fading observed in these cells (see Figure 4a) could be a result of side reactions at the anode consuming cyclable lithium, for example lithium plating, or an incomplete anode delithiation due to the high cell resistance (note that capacity was determined with a constant current C/3 discharge). The low electrolyte fast charge cells (blue closed squares and triangles), however, show only a slight increase in discharge endpoint slippage compared to the low electrolyte C/2 cells (open blue squares,

15% vs. 14% after 130 cycles). Additionally, all cells show a temporary decrease in discharge endpoint slippage after each RPT, which we assign to the formation and partial dissolution of crystalline silicon phase (see below).

Figure 4d shows the average discharge voltage, calculated from the ratio of discharge energy and discharge capacity during the CC phase, of the first cycle of each 3x C/2/C/2 + 3x FC/C/2 sequence. Again, all cells show the same trend of a rising discharge voltage during the first ≈ 20 cycles. After ≈ 20 cycles, the average discharge voltage of the high electrolyte fast charge cells (red closed squares and triangles) declines linearly, indicating an additional overpotential that is not present in neither the low electrolyte cells nor the high electrolyte C/2 cells. The C/2 cells (with both high and low electrolyte, red and blue open squares) show an overall stable average discharge voltage, which is only interrupted by a drop of about 10 mV after each RPT, whereafter the average discharge voltage equilibrates back to the previous value cycles within ≈12 cycles. The average discharge voltage of the low electrolyte fast charge cells (blue closed squares and triangles) also follows this saw-teeth form yet decreases slightly (≈5 mV) during the last 70 cycles.

The saw-teeth shape of both the discharge endpoint slippage (Figure 4c) and the average discharge voltage (Figure 4d) most likely originates from the formation and disappearance of the crystalline $Li_{3.75}Si$ phase:[35,36] During aging cycling (SOC ≥ 10%), lithium is trapped within the crystalline phase, which effectively reduces the usable capacity of the silicon and thus shifts the discharge endpoint slippage and the average cell voltage upwards. The trapped lithium is released again during the full charge/discharge cycles of the RPT (SOC 0%-100%), which is why the cycles directly thereafter show a lower discharge endpoint slippage and lower average cell voltage, until the crystalline phase has formed again. However, our focus in the analysis of the aging cycles (Figure 4c and d) is not the possible occurrence of a crystalline $Li_{3.75}Si$ phase; we rather want to use the discharge endpoint slippage and average discharge voltage as "fingerprinting" techniques with good cycle resolution (6 cycles versus 48 cycles for the RPT data) to demonstrate that whichever process is responsible for the stronger capacity fading and resistance increase in the high electrolyte fast charging cells, it only sets in around cycle ≈20, rather than occurring continuously from the first cycle.

Overall, our results suggest that a distinct failure mechanism occurs in the high electrolyte fast charge cells that comprises high resistance increase (as seen in both the DCIR and the average discharge voltage) and strong capacity decay, resulting - at least partially - from side reactions at the anode, possibly lithium plating. This failure mechanism is not visible in the C/2 cells and strongly diminished in the low electrolyte fast charge cells, although they are cycled under identical conditions. Furthermore, discharge endpoint slippage and average discharge voltage indicate that this failure mechanism only sets in after about 20 cycles. Our findings are in alignment with Bonakdarpour et al.,[15] who also show an enhanced capacity decrease and resistance increase for high electrolyte cells cycled at high C-rates. Finally, we briefly want to mention that the initial (first 50 cycles) capacity loss and resistance increase

observed for the high electrolyte fast-charging cells is largely reversible. This is not shown in Figure 4 and will be discussed in detail later in the manuscript (see Figure 9d and chapter *Capacity & resistance recovery*).

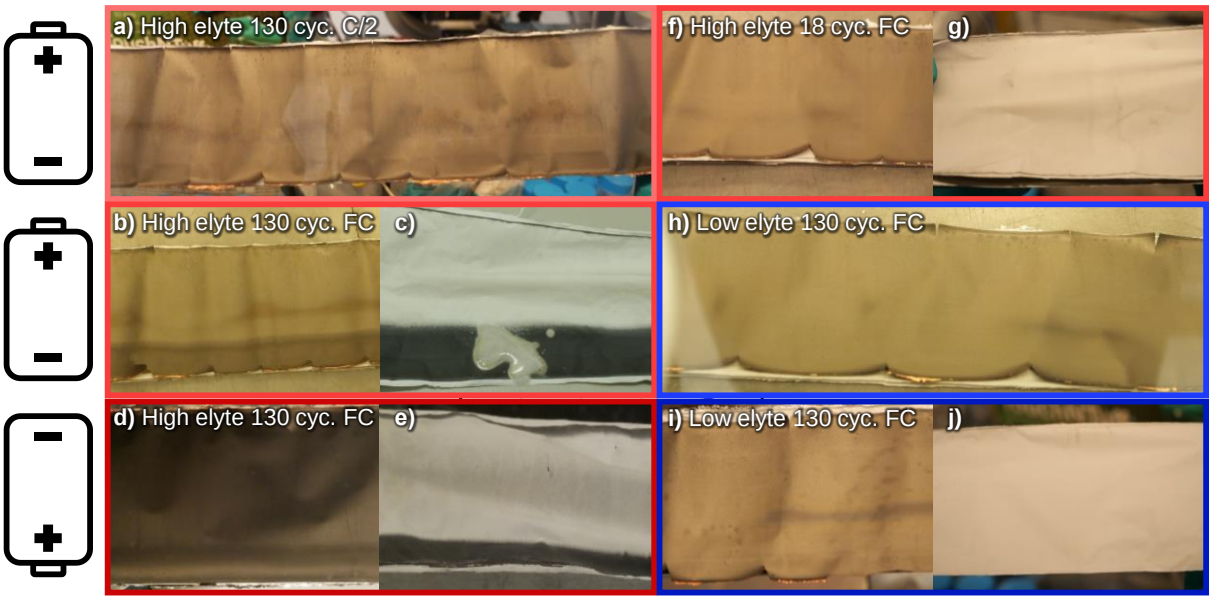

Figure 5 Cell opening of cycled cells and visual inspection for lithium plating on anodes and separators; orientation of images represents cell orientation during cycling. a) Anode of a high electrolyte C/2 cell after 130 cycles; b) anode and c) separator of a high electrolyte fast charge cell after 130 cycles with positive terminal facing up; water was added to the separator to confirm the presence of plated lithium, d) anode and separator of a high electrolyte fast charge cell after 130 cycles with positive terminal facing down; f) anode and g) separator of a high electrolyte fast charge cell after 18 cycles with positive terminal facing up; h) anode of a low electrolyte fast charge cell after 130 cycles with positive terminal facing up; i) anode and j) separator of a low electrolyte fast charge cell after 130 cycles with positive terminal facing down.

After cell cycling, all cells were opened, and electrodes and separators were visually inspected. Figure 5 shows images taken from anodes and separators of selected cells. The high electrolyte C/2 cells (Figure 5a) show no signs of lithium plating on the anode after 130 cycles, as was expected based on the low cycling rate. In contrast, anodes from the high electrolyte fast charge cells cycled with the positive terminal facing up (Figure 5b) show a dark, ≈ 1.5 cm broad stripe at their lower edge (i.e., close to the negative current collector flags) and a less prominent black strip on the upper side, which are both visible over the entire length (≈ 5 m) of the electrode. Identical stripes are present on the separator sides that were facing the anode. Adding a few drops of water to the stripe on the separator resulted in gas formation and a visible clearing (see Figure 5c), which verifies that the dark stripes are indeed plated lithium partially stuck to the separator. Interestingly, the high electrolyte fast charge cells cycled with the positive terminal down (Figure 5d and e) also show a prominent dark stripe at the lower edge of the anode and separator, i.e., towards the positive current collector flags, and a thinner stripe on the upper side. Hence, the location of the prominent lithium plating stripe is not an intrinsic jelly roll property arising from current, temperature, or pressure distribution, as in this case, the stripe should appear at

same location with respect to the current collector in both cells. Rather, the prominent stripe always appears at the side of the jelly roll facing downwards (towards the center of gravity) during cycling.

As our cycling results (Figure 4) indicated that the distinct failure mechanism for the high electrolyte fast charge cells might not be present within the first ≈ 20 cycles, we repeated the fast charge cycling experiment but opened the cells after 18 cycles. Figure 5f and g show the anode and the separator of these high electrolyte fast charge cells opened after 18 cycles. While no lithium plating was visible on the anode, two very thin dark lines can be found on the upper and lower edge of separator facing the anode. This type of lithium plating is commonly seen in large-format lithium-ion cells and possibly comes from a different lithiation degree in the anode overhang.[37,38] However, the prominent lithium plating stripes feature seen in Figure 5b-e were not found in the cells opened after 18 cycles, matching our expectation based on the electrochemical data. Similarly, no signs of plated lithium were found on anodes or separators of the low electrolyte fast charge cells after 130 cycles (Figure 5h-j), irrespective if they were cycled with the positive terminal facing up (Figure 5h) or facing down (Figure 5i and j).

The cell opening confirms that no lithium plating occurs in the first 18 cycles for any cell. After 130 cycles, the high electrolyte fast charging cells show lithium plating along the entire length of the jelly roll, but - independent of cell orientation during cycling - very localized in height and most prominently in a ≈ 1.5 cm broad stripe at the lower anode edge, i.e., the edge that is facing towards the center of gravity.

$LiPF_6$ concentration profiles after cell cycling measured by IC and LC-MS

After visual inspection, we further analyzed extracted electrodes to elucidate the mechanism causing lithium plating on the downward-facing sides of the anodes in the high electrolyte cells (and their absence in low electrolyte cells). We focused on the analysis of electrolyte composition and amount – rather than changes in the active material or electrode structure (e.g., particle cracking, SEI formation, pore clogging etc.) – as the liquid electrolyte is the only component in a lithium-ion cell which we expect to be "responsive" to gravitation. We developed a simple procedure to determine the amount of the conducting salt $LiPF_6$ and the electrolyte solvent ethylene carbonate (EC) at different positions along the jelly roll height ("top vs. "center" vs. bottom"); we focused on spatial resolution along the jelly roll height and not along the length of the electrodes as the lithium plating stripes – wherever present – were found to run along the entire anode length (see Figure 5b-e). In short, jelly rolls were extracted from BOL or cycled cells (24 to 48 hours after the end of active cycling) and the electrodes were separated. While volatile electrolyte components evaporate, $LiPF_6$ and non-volatile EC remained within the electrode pores. Small circular electrode pieces (termed "coins" hereafter) were punched out from the electrodes at different positions along the jelly roll height, $LiPF_6$ and EC were re-dissolved in an extraction solvent and their amounts determined by ion chromatography (IC) and liquid chromatography-mass spectrometry (LC-MS). The determined $LiPF_6$ amounts (in mol) were referenced to the pore volume (in L) of the respective anode/cathode electrode coins to obtain a "pore volume $LiPF_6$

concentration" $c(LiPF_6)$ in units of mol/L_{pore}. The experimentally determined EC amounts (in mol) were referenced to the "expected" EC amount (in mol) and expressed by the value $\alpha(EC) = n(EC)_{measured}/n(EC)_{expected}$ in units of %. The expected EC amount is calculated based on the EC volume share in the electrolyte and the electrode pore volume. A detailed description of the electrolyte extraction procedure and further details on the electrode specific pore volume calculation (in difference to the above-described total pore volume calculation) are given in the Methods Section.

Figure 6 shows the experimentally determined $LiPF_6$ (red/blue curve, lower x-axis) and EC concentration profiles (orange/cyan, upper x-axis) along the jelly roll height of the cells for high (Figure 6a-e) and low electrolyte (Figure 6f-j) cells opened at BOL, after fast charging and C/2 cycling. Before we turn to the results, let us briefly take a closer look at the data basis for the $LiPF_6$ concentration values. Both anodes and cathodes were sampled and their Li^+- (IC) and PF_6^--concentration (IC and LC-MS) were determined independently. The Li^+- and PF_6^--concentrations determined from IC measurements were identical within ± 5% within each sample (with a few exceptions as explained in the Methods Section), which is a physical necessity to maintain local charge neutrality within the electrolyte, and thus were averaged to obtain a single $LiPF_6$ concentration for each sample. Also, $LiPF_6$ concentrations were very similar in anodes and cathodes sampled in the same jelly roll height position; this is because the distance between anode and opposing cathode is very short (order of magnitude of 100 – 200 µm) and therefore any local anode-cathode concentration gradient fully equilibrates during the 24 to 48 rest time prior to cell opening. Therefore, we also averaged anode and cathode $LiPF_6$ concentrations into one single value, which is displayed in Figure 6; the error bars in Figure 6 represent the standard deviations of two cells and several anode and cathode values (details on underlying individual sample numbers are given in Table S1 in the Supporting Information). For cells opened after 130 cycles (Figure 6c-e and h-j) there are two differences in the $LiPF_6$ data basis in comparison to the BOL and 18 cycle cells (Figure 6a, b, f and g): i) in some cells, lithium plating prohibits a proper separation of the anode from the separator, therefore we only sampled cathodes (for all 130 cycle cells, also if no lithium plating occurred), which reduces the amount of individual samples by a factor of two but is otherwise unproblematic as anode and cathode $LiPF_6$ concentrations are identical as mentioned above; ii) we only state $LiPF_6$ concentrations (in mol/L_{pore}) for three positions (very top/bottom and center) in contrast to five positions for the BOL and 18 cycle cells due to a missing LC-MS $LiPF_6$ calibration curve for the 130 cycle cells. The omitted data for the other two positions is displayed in Figure S6 in the Supporting Information in a semi-quantitative way (normalized to the center position) and matches the profile shapes shown in Figure 6c-e and h-j.

Let us first consider the $LiPF_6$ profiles of the high electrolyte cells. For the BOL cell (Figure 6a), the $LiPF_6$ concentration is close to ≈ 1.25 mol/L_{pore} (indicated by dashed black vertical line) for all positions except the very top and bottom. This is exactly the concentration which one would expect for the BOL electrolyte, as the pristine electrolyte (before formation) had a $LiPF_6$ concentration of 1.2 mol/L_{pore} and

around 5% of the solvent is expected to be lost during formation (as already discussed above). At the very top and bottom the $LiPF_6$ concentrations deviate from the ideal value of 1.25 mol/L_{pore}; this is probably an artefact from electrolyte filling and/or cell formation and of no further importance. After 18 fast charge cycles, the $LiPF_6$ concentration profile has already changed dramatically (Figure 6b). In the center position, the $LiPF_6$ concentration has increased to ≈ 1.7 mol/L_{pore} while it has decreased to ≈ 0.5 mol/L_{pore} and ≈ 1.0 mol/L_{pore} at the upper and lower edges, respectively; this corresponds to a change of ≈ 60% at the bottom position after only 18 cycles!

After 130 cycles of the fast-charging protocol, the $LiPF_6$ concentration has increased to ≈ 1.7 mol/L_{pore} at the center and ≈ 1.3 mol/L_{pore} at the upper edge, while it has decreased to < 0.1 mol/L_{pore} at the lower edge (Figure 6c). This is an even more profound change as the ionic conductivity will decrease tremendously at such a low $LiPF_6$ concentration.[39,40] After 130 cycles at C/2 (Figure 6d), the $LiPF_6$ concentration profile looks qualitatively similar but is quantitatively less extreme with a center concentration of ≈ 1.3 mol/L_{pore}, and ≈ 0.5 mol/L_{pore} and ≈ 1.1 mol/L_{pore} at the bottom and top edges, respectively. This is a clear indication that the build-up of the concentration gradient increases with higher charging C-rate.

Finally, Figure 6e shows the $LiPF_6$ concentration profile after 130 fast charging in high electrolyte cells which were cycled with their positive terminal facing down. Here, the $LiPF_6$ concentration has increased to ≈ 2.5 mol/L_{pore} at the center and decreased to < 0.1 mol/L_{pore} and 0.7 mol/L_{pore} at the bottom and top edges, respectively. Figure 6c and e demonstrate that the lowest $LiPF_6$ concentration always occurs at the bottom position, irrespective of whether the positive terminal was facing up (Figure 6c) or down (Figure 6e). For both orientations, the occurrence of lowest $LiPF_6$ concentrations at the bottom edge matches with the prominent lithium plating stripes which also developed on downward-facing anode sides (see Figures 5b-e). Interestingly, the concentration profiles for the two orientations are not perfectly mirrored around the electrode center though; we attribute this asymmetry to different electrolyte flow patterns as discussed later.

What is the source of this dramatic local deviation of the $LiPF_6$ concentration for the high electrolyte cells? At this point it is important to recall that Figure 6 displays $LiPF_6$ concentrations in units of mol/L_{pore}, not mol/$L_{electrolyte}$. In theory, a difference in $c(LiPF_6)_{pore}$ concentration can be due to i) a difference in electrolyte pore filling ("higher or lower electrolyte volume") or ii) a difference in electrolyte salt concentration (in mol/$L_{electrolyte}$). While a change in local electrolyte amount could explain a deviation towards lower $LiPF_6$ concentrations due to a partial electrode dry out, it cannot explain $LiPF_6$ concentrations above the initial 1.25 mol/L_{pore}, because this concentration (in mol/L_{pore}) already corresponds to a local pore filling ratio of 1.0 and the electrolyte volume can – obviously – not exceed the pore volume. Therefore, the fact that we observe $LiPF_6$ concentrations of up to ≈ 2.5 mol/L_{pore} is a clear indication for a "true" $LiPF_6$ concentration gradient (in mol/$L_{electrolyte}$) in the liquid electrolyte.

To further substantiate this argument, we also attempted to measure the spatial distribution of the electrolyte solvents. Unfortunately, we did not succeed in getting reliable values for the volatile linear carbonates due to their rapid evaporation (see Figure S5 in Supporting Information) and could only determine local amounts of the non-volatile EC. For the BOL and 18 cycle fast charge cells (Figure 6a and b, orange curve and upper x-axis), the *α(EC)* values are close to 100% in all positions; a value of 100% indicates that the experimentally determined EC amount is close to the EC amount expected based on the BOL electrolyte composition and pore volume. The cells after 18 cycles (Figure 6b) are especially instructive as they already exhibit a significant $LiPF_6$ concentration gradient but display a very constant *α(EC)* profile which further supports the presence of a "real" $LiPF_6$ concentration gradient in the liquid, rather than a local change in electrolyte pore filling.

After 130 cycles (Figure 6c-e), the *α(EC)* profiles change a little (in comparison to the $LiPF_6$ concentration profiles) with the lowest *α(EC)* value of ≈ 60% for the bottom position after 130 cycles of fast charging in an upright position (Figure 6c). This might be due to i) a partial electrode dry-out or ii) a change in electrolyte composition due to preferential EC consumption at the anode (remember that these cells already exhibit significant lithium plating). Either way, at this position only 40% of the EC has been lost, while the $LiPF_6$ loss amounts to more than 90% (< 0.1 mol/L vs. 1.25 mol/L), meaning that although we cannot (and do not want to) rule out some additional electrode dry out after extended cycling, the dominant reason for the low $LiPF_6$ amount is indeed a decrease in liquid electrolyte $LiPF_6$ concentration (in $mol/L_{electrolyte}$).

Let us now turn to the low electrolyte cells shown in Figure 6f to j. For the low electrolyte cells (Figure 6f) we find a BOL $LiPF_6$ concentration of ≈ 1.1 mol/L_{pore} which compares to ≈ 1.25 mol/L_{pore} for the high electrolyte BOL cells (Figure 6a); this lower $LiPF_6$ concentration (in mol/L_{pore}) reflects the incomplete pore filling at 0% SOC (at which cell opening occurred) for the low electrolyte cells and not a lower electrolyte concentration (in $mol/L_{electrolyte}$). Looking at the cycled low electrolyte cells (Figure 6g to j), the main findings are i) that qualitatively there is the buildup of triangular $LiPF_6$ concentration profiles with highest concentrations in the center and lowest concentrations at the edges but ii) quantitatively these profiles are much "flatter" and less extreme than those in the high electrolyte cells. In the low electrolyte cells, the lowest $LiPF_6$ concentration equals 0.8 mol/L_{pore} (Figure 6h, top and bottom position) which compares to < 0.1 mol/L_{pore} for the respective high electrolyte cell (Figure 6c, bottom position).

The *α(EC)* profile for the BOL low electrolyte cells is flat and centers around ≈ 105% (Figure 6f), which compares to ≈ 115% for the BOL high electrolyte cell (Figure 6a); the lower value for the low electrolyte cell is due to lower pore filling ratio, following the same logic explained above for the $LiPF_6$ concentration (in mol/L_{pore}). The *α(EC)* profiles for all cycled cells (Figure 6g to j) show hardly any change in comparison to the BOL cells (Figure 6f); this is simply a consequence of the low amount of side reactions in the low electrolyte cells as indicated by the absence of any significant lithium plating

(Figure 5), and thus the absence of partial electrode dry out and/or EC reduction as observed for the high electrolyte cells.

The main findings of this section are:

1) High electrolyte cells rapidly develop a strong $LiPF_6$ concentration gradient in the liquid electrolyte upon cycling, especially when applying high charging C-rates.
2) For high electrolyte cells, the lowest $LiPF_6$ concentrations always occur on the bottom side (facing downwards during cycling) which matches the position of the dominant lithium plating stripe.
3) The high electrolyte fast charging cells opened after 18 cycles already show a significant $LiPF_6$ concentration gradient, but no significant lithium plating. This demonstrates that the $LiPF_6$ concentration gradient precedes lithium plating and abnormalities in discharge endpoint slippage and average discharge voltage, not vice versa.
4) Low electrolyte cells in which no significant electrolyte motion occurs do not develop a significant $LiPF_6$ concentration gradient.

To the best of our knowledge, this is the first experimental demonstration of a significant $LiPF_6$ concentration gradient on a cm-scale in cycled lithium-ion cells. It is astonishing that such a fundamental behavior has been overlooked so far. This might be because such a “spontaneous de-mixing” of the electrolyte is highly counter-intuitive as it seems to violate the second law of thermodynamics. In the next sections we will first suggest an underlying mechanism and then discuss the far-reaching implications of this concentration gradient.

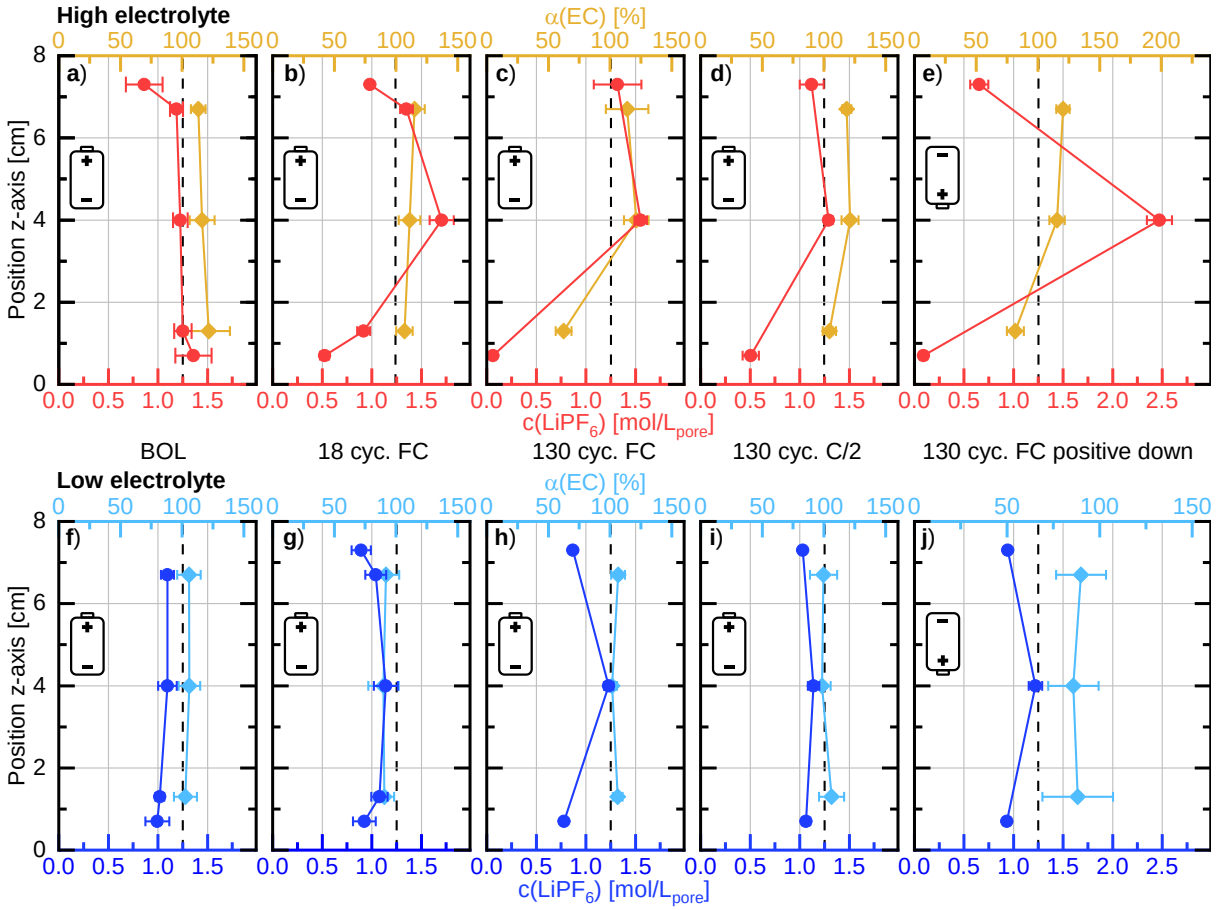

Figure 6 $LiPF_6$ concentrations (red/blue, lower x-axis) and *α(EC)* profiles (orange/cyan, upper x-axis) for high (a-e) and low electrolyte (f-j) cells at begin of life (a, f), after 18 (b, g) and 130 cycles fast charging (c, h), 130 cycles C/2 cycling (d, i) and 130 cycles fast charging with the positive terminal facing down (e, j). The dashed black line in each panel indicates the expected value of $c(LiPF_6)$ = 1.25 mol/L and α(EC) = 100%; error bars indicate the standard deviation of multiple individual measurements (see Supporting Information for details on sample size).

Mechanistic origin the $LiPF_6$ concentration gradient

In the previous section we have demonstrated that the high electrolyte cells rapidly develop a strong $LiPF_6$ concentration gradient along the cell height, which is accompanied by capacity decrease, resistance increase and localized lithium plating at the bottom side of the anode. The sensitivity towards gravitation and the absence of the $LiPF_6$ concentration gradient in the low electrolyte cell point towards a central role of electrolyte motion. In this section, we will suggest a mechanism for how electrolyte motion could cause the observed $LiPF_6$ concentration gradient.

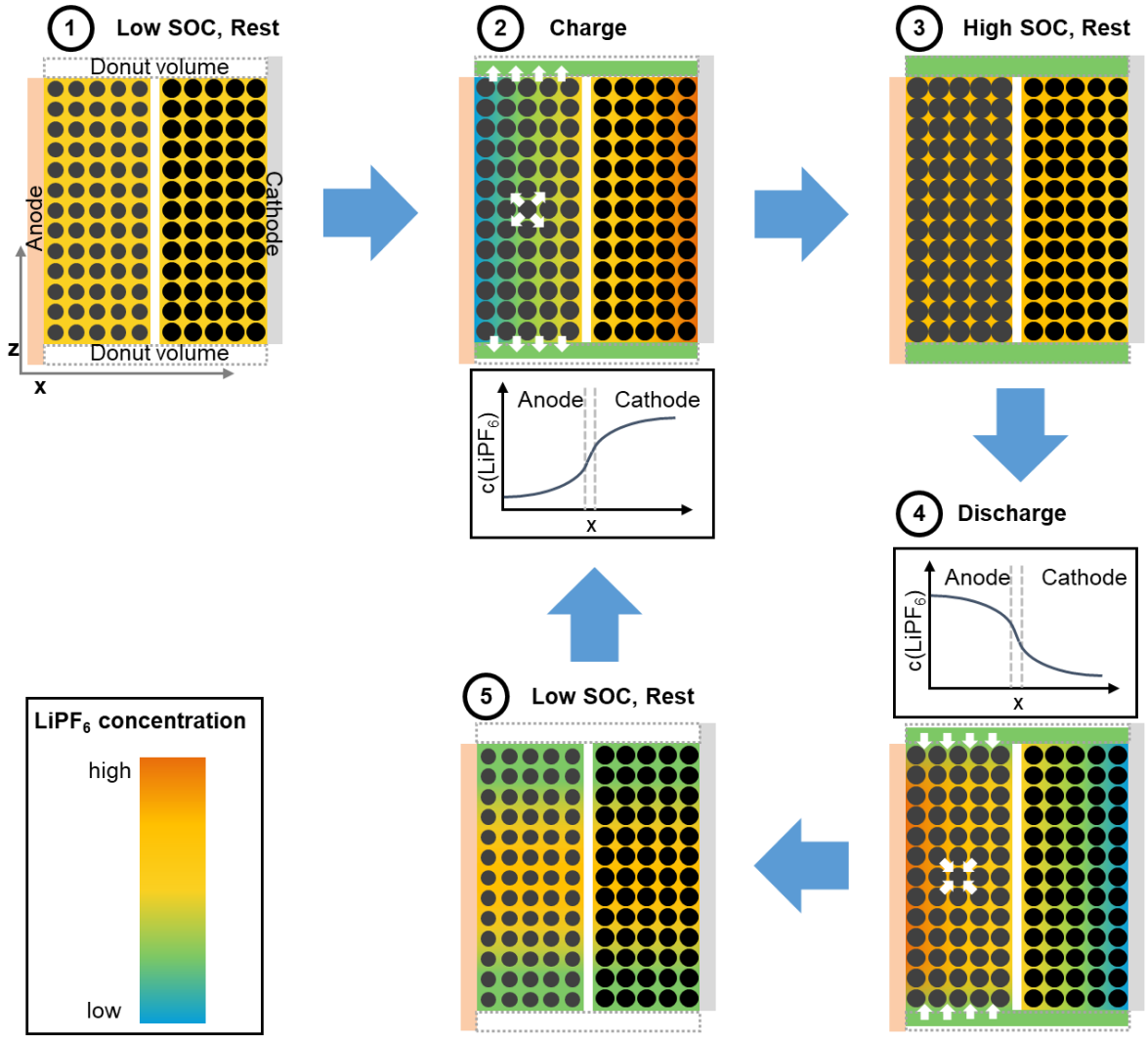

Figure 7 Proposed mechanism for how electrolyte motion causes an in-plane (= along the z-axis) $LiPF_6$ gradient along the jelly roll height; note that the depicted scales for x and z-axis are different (x-axis ≈ 100-200 µm, z-axis ≈ 1-10 cm depending on cell dimension); the color shading depicts the $LiPF_6$ concentration in the liquid electrolyte inside the porous electrodes and (where present) in the donut volume.

Figure 7 shows a schematic of a single charge-discharge cycle of one anode/separator/cathode layer with an electrolyte volume that fills the entire porosity already at low SOCs, i.e., similar to our high electrolyte 4695 cells. (1) The cell is well-equilibrated at rest at low SOC (e.g., 10% SOC), all pores in the jelly roll are filled with electrolyte with a homogeneous $LiPF_6$ concentration (indicated by color

shading) and the donut regions above and below the jelly roll are empty. (2) A high charging current is applied, causing a concentration gradient in the liquid electrolyte in x-direction, i.e., through-plane with regard to anode and cathode, as lithium-ions are intercalated into the anode active material and de-intercalated from the cathode active material. This through-plane concentration gradient, which is well established and can be reproduced by any p2D-type electrochemical simulation, is steeper at higher currents (i.e., during fast charge). At the same time, the anode active material expands with increasing cell SOC, causing a net in-plane electrolyte flow from the jelly roll into the donut volume. Our crucial (and yet unproven) assumption is that the electrolyte flow out of the jelly roll originates not equally from anode and cathode but preferentially from the anode, as the electrolyte flow will take the path of lowest resistance. We assume that the higher porosity and the preferential in-plane orientation of flake-shaped graphite particles results in a higher in-plane electrolyte permeability of the anode coating compared to the cathode coating, which is comprised of spherical particles and has a lower porosity. If this assumption holds true, the concurrency of the through-plane concentration gradient with the preferential flow of anode electrolyte causes the motion of $LiPF_6$-depleted electrolyte towards the donut region. (3) Once the (fast) charge has terminated, the current-driven through-plane concentration gradient between anode and cathode equilibrates (typically within minutes due to the short diffusion length of ~100 µm) to a $LiPF_6$ concentration slightly higher than the initial value within the jelly roll, while the $LiPF_6$ concentration in the free electrolyte in the donut region remains below the initial $LiPF_6$ concentration. (4) During subsequent discharge, the anode active materials contracts and electrolyte flows back from the donut region into jelly roll. Additionally, the current-driven through-plane gradient is now reversed, i.e., the anode electrolyte contains a higher $LiPF_6$ concentration, while the electrolyte in the cathode has a lower $LiPF_6$ concentration. Due to the postulated higher anode coating in-plane permeability, the in-plane electrolyte flow towards the jelly roll center again takes place preferentially through the anode; therefore, the jelly roll center is filled with $LiPF_6$ enriched electrolyte, while the jelly roll edges are refilled with $LiPF_6$ depleted electrolyte from the donut region. (5) After the discharge is completed, all electrolyte has flown back into the jelly roll, and the donut volume is empty. However, along the height of the cell, a $LiPF_6$ gradient in the in-plane direction, with low concentration at the edges and high concentration in the jelly roll center, is now present. Because concentration differences in through-plane direction equilibrate quickly once no current is driven, this gradient in salt concentration along the cell height can be found in both the anode and the cathode electrolyte. During the next cycle, the process is repeated, and the $LiPF_6$ concentration between jelly roll center and edge at the end of the cycle will diverge further. In this way, continuous cell cycling at high C-rates leads to a depletion of salt at the jelly roll edge, while the electrolyte in the jelly roll center will be enriched.

Essentially, according to this proposed mechanism, the $LiPF_6$ concentration gradient along the cell height is created by classical through-plane electrochemistry on a µm-scale and perpetuated onto the cm-scale by concurrent in-plane electrolyte motion.

Electrochemical simulation linking the $LiPF_6$ concentration gradient to local lithium plating

To assess how fast a substantial $LiPF_6$ concentration gradient would occur in case of different anode and cathode permeabilities, and to understand its effect on the likelihood of lithium plating, we employed an electrochemical simulation that was designed to capture the mechanism depicted in Figure 7. We combined a simplified 2D Doyle-Fuller-Newman model[41,42] consisting of a single anode/separator/cathode layer with an electrolyte flow model (see Methods section for details). For simplification, we assumed symmetry along the center plane of the jelly roll (see Figure 8a). The model incorporates the swelling of anode particles during intercalation, resulting in a decrease in porosity. Consequently, the electrolyte is expelled from the jelly roll into an expandable donut volume during battery charging, and this process is reversed during discharge. In accordance with the above suggested mechanism, the in-plane permeability of the anode towards electrolyte flow was adjusted to be 3-fold of the cathode permeability. Further model parameters were taken from literature (see Methods section for details); although some parameters do not fully match our experimental cells in terms of base electrolyte concentration, cell chemistry, electrode thickness etc., we chose these parameters to provide full transparency and to allow fellow researchers to reproduce these findings. In this sense, the simulation does not target to capture the experimental results in a quantitative way, but rather to highlight the qualitative effects of a higher permeability in the anode over several cycles. In total, 30 cycles were simulated using the same 3x C/2/C/2 + 3x FC/C/2 sequence with the same fast charge profile employed in the experimental cell cycling (see Figure 4 and S3).

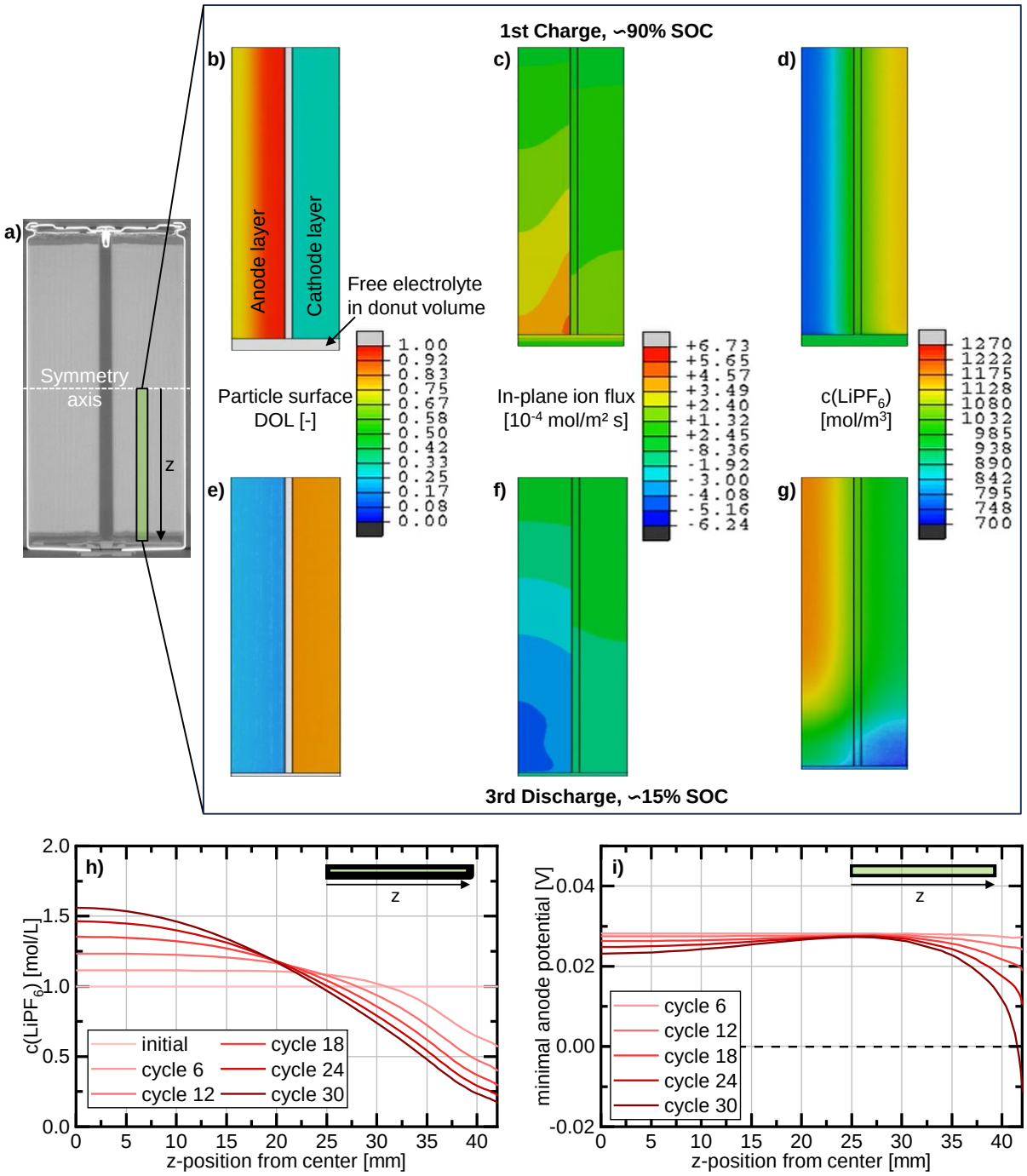

Figure 8 Simulation results of a simplified 2D electrochemical model coupled with in-plane electrolyte flow. a) Symmetry along the center plane was employed as a boundary condition; b-g) snapshots of the lithiation degree at particle surface, in-plane ion flux and $LiPF_6$ concentration in the electrolyte during the first charge at ≈ 90% SOC (b-d) and during the 3rd discharge at ≈ 15% SOC (e-g) of 3 charge/discharge cycles. A video of all three cycles can be found in the supporting information. h) $LiPF_6$ concentration (averaged across through-plane direction) along the z-dimension after discharge + 10 min rest for selected cycles. i) Minimal anode potential at ≈ 65% SOC along the z-dimension during fast charging for selected cycles.

Figure 8 shows snapshots of the simulation results for surface particle lithiation degree (b, e), in-plane ion flux (c, f) and $LiPF_6$ concentration in the electrolyte (d, g). During the first charge, lithium ions are intercalated into the anode particles (Figure 8b), and as expected, a gradient in $LiPF_6$ salt concentration builds up, exhibiting the lowest concentration at the anode close to the current collector and the highest

concentration close to the cathode current collector (Figure 8d). The in-plane ion flux (Figure 8c) induced by particle swelling has a positive sign, indicating that electrolyte is pressed out of the jelly roll and into the expandable donut volume, causing the latter to expand accordingly. As a direct result of the assumed permeabilities (three times higher in the anode), most of the in-plane ion flux passes through the anode. Note that the in-plane ion flux is largest at the electrode edge towards the donut volume, as the flow accumulates over the jelly roll length, while the in-plane ion flux at the jelly roll center equals to zero due to the symmetry condition at the upper boundary. During the 3rd discharge, the particle lithiation (Figure 8e) and the through-plane $LiPF_6$ concentration gradient (Figure 8g) show, as expected, an inversed behavior. Also, the in-plane ion flux switches its direction (Figure 8f), which means that electrolyte is soaked back into the jelly roll. Notably, an in-plane gradient in $LiPF_6$ concentration spreading from the lower electrode edge can be seen (Figure 8g). This gradient is characterized by an elevated concentration at the center of the jelly roll, while a reduced concentration is observed in the donut volume and at the edge of the jelly roll. Overall, the simulations show the same behavior as described schematically in Figure 7, proving that the combination of rigid clamping, electrolyte motion and unequal electrode permeabilities inevitably leads to the formation of an in-plane $LiPF_6$ concentration gradient over the jelly roll height.

Figure 8h shows how this in-plane concentration gradient builds up over 30 cycles (5 repetitions of the 3x C/2/C/2 + 3x FC/C/2 sequence) to a bell-shaped profile. After 30 cycles, the average $LiPF_6$ concentration at the electrode edge has decreased to almost 0.2 mol/L, while the concentration in the jelly roll center has continuously increased from 1.1 mol/L after cycle 6 to 1.6 mol/L after cycle 30. This trend is in good agreement with our experimental findings (see Figure 6), considering that we purposely chose a cell parameter set for the simulation that does not fully match our 4695 cells.

To better understand why the lithium plating in our experimental cells correlated with areas of low electrolyte concentration, Figure 8i shows the minimal anode potential at ~65% SOC along the cell z-axis during fast charging. While during cycle 6, the minimal anode potential is constant around 28 mV along the z-direction and far away from 0 V vs. Li/Li^+ (i.e., the onset of lithium plating), the minimal anode potential at the jelly roll edge decreases continuously over 30 cycles, until it eventually falls below 0 V. Accordingly, with a $LiPF_6$ gradient evolving over the jelly roll height, lithium plating can occur at the jelly roll edge, even if the same fast charge profile would not lead to lithium plating on a fresh cell. Interestingly, the anode potential in the center also decreases, albeit to a lesser extent. We attribute this behavior to the following reasons: Firstly, typical $LiPF_6$ containing electrolytes exhibit a conductivity maximum at a concentration of approximately 1-1.3 mol/L.[39,40] With significant deviation in $LiPF_6$ from this ideal value, the mass transport in the electrode pores becomes slower. This results in particles located further away from the separator interface absorbing less lithium-ions. The surplus charge (per area) is redistributed to the particles in closer proximity to the separator interface, hence leading to a higher local C-rate. Secondly, also the kinetics at the electrolyte-particle interface are influenced by the

local $LiPF_6$ concentration, as the charge transfer resistance becomes higher for $LiPF_6$ concentrations that deviate significantly from ≈ 1 mol/L.[43] As a result, the anode potential upon fast charging is slightly reduced in regions with increased $LiPF_6$ concentration (i.e., jelly-roll center) and significantly reduced in regions with decreased $LiPF_6$ concentration (i.e., jelly-roll edges).

The simulations show that a) the mechanism proposed in Figure 7 (electrolyte motion → in-plane $LiPF_6$ gradient) can be reproduced by physics-based simulations using reasonable boundary conditions under the assumption of unequal anode/cathode in-plane permeabilities and that b) the experimentally found in-plane $LiPF_6$ gradient can cause lithium plating in areas with low $LiPF_6$ concentration. We want to stress that the latter causation (in-plane $LiPF_6$ gradient → local lithium plating, see Figure 8h and i) holds true independent of the actual mechanism of how electrolyte motion leads to a $LiPF_6$ gradient. In summary, we consider this sequence of "electrolyte motion → in-plane $LiPF_6$ gradient" as a novel and specific mechanism of high importance for large format lithium-ion cells, which we suggest naming *electrolyte motion induced salt inhomogeneity* (EMSI). This EMSI effect has several further implications which will be discussed in the following sections.

Implications for cell design

Active material choice. – The strength of the EMSI effect is expected to increase with increasing total volume change of anode and cathode active materials upon charging and discharging, making it especially relevant for silicon-containing cells. However, we have already observed the EMSI effect taking place in other cell types containing graphite as the only anode active material (data not shown). In contrast, if the SOC-dependent volume changes of the different active materials largely cancel out (e.g., lithium titanate oxide versus a mixture of lithium cobalt oxide and NMC),[44] the EMSI effect is not expected to take place at a significant scale.

Electrode design. – The design of the battery electrodes (including active material loading, porosity, tortuosity, particle shape and orientation and more advanced micro-structuring techniques) has been optimized for decades to improve energy density, power capability and lifetime. So far, these design efforts mostly focused on improving the *through-plane* transport of lithium-ions in the immobile liquid electrolyte between anode and cathode (with the noteworthy exception of electrolyte filling studies).[45–47] Considering the EMSI effect, also *in-plane* electrode properties, especially in-plane electrolyte permeability (which is probably related to in-plane tortuosity),[48] will become relevant parameters requiring further method development. Based on our mechanistic understanding, we predict that equalization of anode and cathode permeabilities will eliminate the EMSI effect, while increasing the cathode permeability above that of the anode will even lead to an "inversed" EMSI effect with $LiPF_6$ depletion in the jelly roll center. The addition of the in-plane dimension will make design choices such as balancing of anode versus cathode porosities and in-plane versus through-plane electrode tortuosities significantly more complex.

Nevertheless, increasing the "classical" through-plane lithium-ion transport will also indirectly reduce the EMSI effect, as it reduces the conducting salt polarization during charge and discharge displayed in steps 2 and 4 in Figure 7; therefore, we expect high energy cells to be generally more affected by the EMSI effect than high power cells.

Electrolyte amount and formulation. - The EMSI effect makes the electrolyte volume a key design parameter for large format lithium-ion cells. In this study we have demonstrated that lowering the pore filling ratio to < 1.0 at 100% SOC effectively suppresses the EMSI effect. This is probably the mechanistic origin of the adverse "high volume effect" recently described by Bonakdarpour et al.[15] In our study, the low electrolyte cells first and foremost serve as a proof of concept to support the EMSI mechanism, but the good fast charging performance (see Figure 4) raises the question of whether such a low electrolyte amount could also be feasible design choice for lithium-ion cells. The obvious disadvantages of low electrolyte amounts are the higher overall cell resistance (see Table 1) and especially the risk of reduced lifetime upon extended cycling or calendaric ageing due to electrolyte consumption.[49–51] Furthermore, the electrolyte amount will also influence flow patterns inside the cell as discussed below.

Electrolyte composition. – Following up on the in-plane $LiPF_6$ gradient, the question remains whether electrolyte solvent segregation also occurs along the jelly roll height. Wang et al.[52] have recently described that solvent segregation occurs in parallel with the conducting salt concentration gradient in the through-plane direction (i.e., between anode and cathode) and found a positive correlation between $LiPF_6$ and linear carbonate concentration and a negative correlation between $LiPF_6$ and EC concentration. Coupling of such a through-plane solvent gradient with the in-plane electrolyte motion might eventually lead to an increased EC concentration at the jelly roll edge and an increased DMC concentration in the jelly roll center. Unfortunately, our limited data on the spatial distribution of different solvent components (see discussion above and Supporting Information) does not allow to properly assess this hypothesis. A similar "anion segregation" might also occur if a dual-salt electrolyte was used, comprised of two (or more) anions with different ionic mobilities. Further research is needed to validate or reject these hypotheses.

Cell format. – Fundamentally, the EMSI effect can occur in any cell in which significant internal pressure prevents electrode breathing and therefore causes electrolyte motion due to reversible pore volume reduction and expansion.[53,54] This also applies to prismatic and pouch cells in most practical applications where limited space available for cell expansion due to geometric constraints (e.g., in a module frame). We have initial experimental data which proves the existence of the EMSI effect in large-format prismatic cells when cycled under high external pressure, which will be published in a separate study in the near future. In this sense, the high electrolyte cells used in this study are very susceptible for the EMSI effect, as they combine active materials with large volume expansion (i.e., silicon), low electrode porosity (and thus low permeability) especially in the cathode, a pore filling ratio > 1 and a cell format which does not allow any electrode expansion. While many of today's commercial

cells will differ in one or more of these parameters from our cells, making them less prone to the EMSI effect, the EMSI effect must be considered for the design of future high energy density lithium-ion cells.

Implications of electrolyte flow patterns

In the previous two sections we showed that the $LiPF_6$ concentration gradient develops in parallel to the direction of electrolyte flow. Therefore, the shape of the $LiPF_6$ concentration gradient within the jelly roll depends on the actual flow pattern within a given cell. To the best of our knowledge, there are no published reports on electrolyte flow patterns in lithium-ion cells (with the exception of a recent conference contribution by Dahn and co-workers[55]), so we want to briefly discuss two conceivable flow patterns which might explain the different $LiPF_6$ profiles observed in the high electrolyte cells with the positive terminal facing either up or down (see Figure 6c and e).

The most simple scenario is depicted in Figure 9a, in which electrolyte is pressed out symmetrically during charge (yellow arrows), stored in the upper and lower donut regions and then flows back the same way during the subsequent discharge (blue arrows). For this electrolyte flow pattern, the EMSI effect has an identical impact on both sides of the jelly roll, giving rise to a symmetrical and triangular conducting salt concentration profile, similar to the one observed for the high electrolyte cell cycled with the positive terminal facing down (Figure 6e). Note that such a symmetric flow pattern also emerges in the simulations depicted in Figure 8.

A more complex scenario is shown in Figure 9b; here, the electrolyte which was pressed into the upper donut region upon charge is not retained there, but flows downwards through the hollow core. At the end of charge, all "free" electolyte (= outside of jelly roll porosity) is present in one single reservoir in the lower donut region and/or the bottom of the hollow core. During the subsequent discharge, the entire jelly roll has to be resupplied from this reservoir (as the upper donut volume is empty), leading to an asymmetric flow pattern. It is quite challenging to properly asses how such a complex electrolyte flow pattern would affect the conducting salt concentration profile in detail. We assume that the $LiPF_6$ concentration will be the lowest in that part of the jelly roll which is directly refilled by free electrolyte, as the free electrolyte is $LiPF_6$-depleted in comparison to the jelly roll average. Therefore, the electrolyte flow pattern depicted in Figure 9b will most likely result in an asymmetric conducting salt gradient with the lowest concentration at the bottom side (facing towards center of gravity), similar to the one which we detected in the high electrolyte cells cycled with the positive terminal facing upwards (see Figure 6c).

To obtain the symmetric flow pattern depicted in Figure 9a, the upper donut region i) must have a void volume large enough to contain all electrolyte pressed upwards and ii) provide sufficient capillary forces or be "tightly sealed" towards the hollow core to prevent the electrolyte from flowing downwards. If either of these two conditions is not fully met, a certain fraction of the electrolyte will flow downwards, shifting the character of the flow pattern towards the asymmetric scenario shown in Figure 9b. The two

scenarios (Figures 9a and b) can be considered as the two ends of a continuous spectrum with an electrolyte retention in upper donut region of 100% and 0%, respectivley.

Why would a symmetric flow pattern (Figure 9a) occur in our 4695 cells cycled with their positve terminal facing down and a asymmetric flow pattern (Figure 9b) in the cells cycled with their positive terminal facing up? While we have no definite proof, we suggest that the different flow patterns might be caused by the electrolyte sealing pin (visible as bright object at upper end of hollow core in Figure 9a) at the negative terminal side, as it potentially reduces the electrolyte flow from the upper donut region into the hollow core on the anode side. We consider the elucidation of electrolyte flow patterns to be an important field for further studies requiring significant additional research and method development. We also want to note that a variety of different flow patterns different from the two suggestions in Figure 9a and b are conceivable, especially for large-format prismatic and pouch cells with different stack/jelly roll geometries.

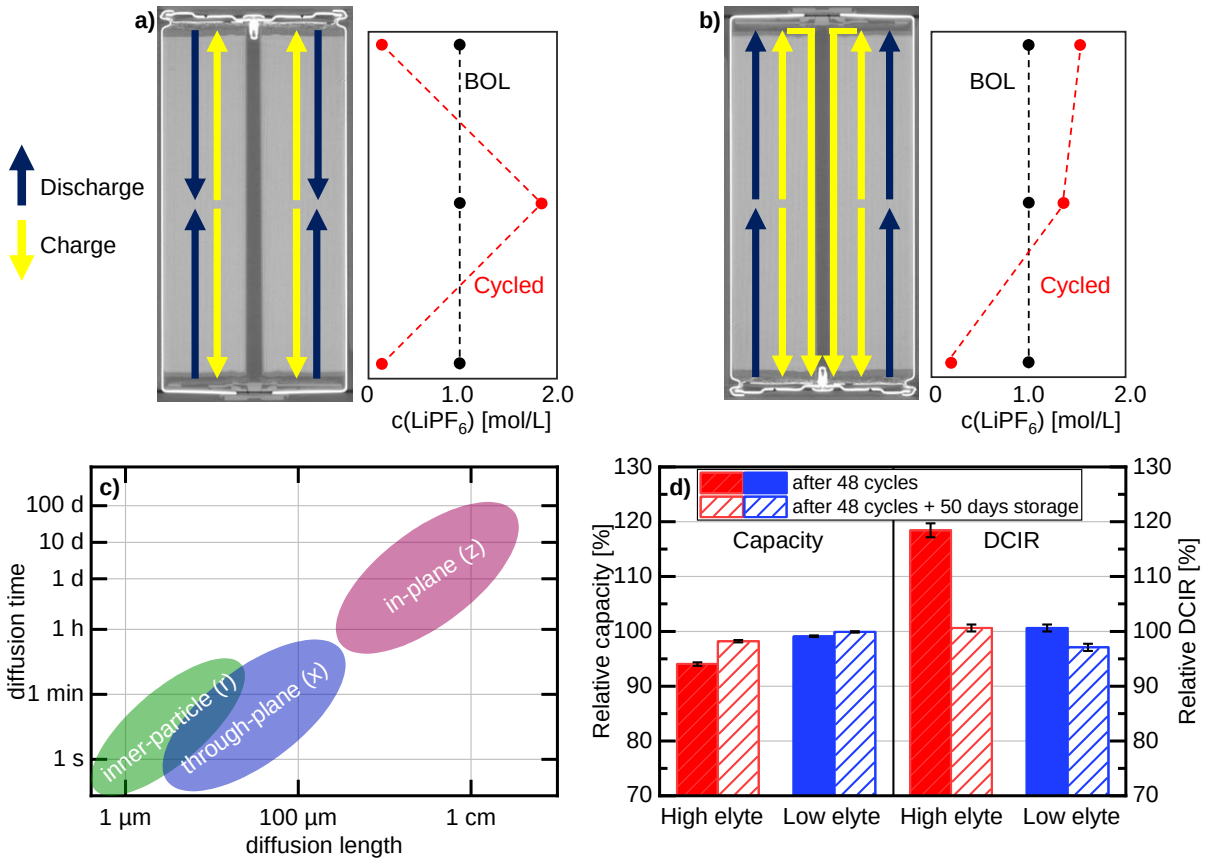

Figure 9 a) Symmetric electrolyte flow pattern (left panel) in which upper donut region retains the electrolyte and schematic of corresponding conducting salt concentration gradient (right panel); b) like a) for asymmetric electrolyte flow pattern in which electrolyte is not retained in the upper donut region but flow downwards through hollow core; c) time-scales for equilibration of lithium-ion concentration gradients within active material particles (green area) and in the liquid electrolyte in the through-plane (blue area) and in-plane direction (purple area) as a function of the characteristic length scales; d) cell capacity (left panel, C/3, 25 °C) and DCIR (right panel, 30 s 2C discharge pulse at 50% SOC, 25 °C) of high (red) and low (blue) electrolyte cells determined in a RPT directly after 48 fast charge cycles (solid bars) and in a second RPT after 50 days additional days of storage at 0% SOC (dashed bars).

Implications for lifetime testing

Cycling parameters. –Let us now consider how common cycling parameters influence the EMSI effect. Increasing the cycling C-rate enhances the severity of the EMSI effect due to a stronger through-plane concentration gradient (step 2 and 4 in Figure 7); in this study we only demonstrate this for the charging C-rate (compare Figure 6c and d), but based on our mechanistic understanding the same holds true for discharging C-rates. However, we would like to point out that an irreversible cell deterioration only occurs if the cell is driven into lithium plating due to the EMSI effect. In the present study, we have deliberately used a very aggressive fast-charging time to create a strong and easily discernible EMSI effect. For the high electrolyte fast-charging cells, strong lithium-plating and capacity fading occurs once a sufficient in-plane salt gradient has developed. Nevertheless, also the high electrolyte cells cycled with a more moderate C/2 charging rate exhibit a significant in-plane concentration gradient after 130 cycles, but in this case the EMSI effect does not cause lithium plating due to the lower charging C-rate. Accordingly, an in-plane salt gradient might not be truly "harmful" as long as charging is limited to moderate C-rates, and the respective cell might run for hundreds or even thousands of cycles. Following the same logic, decreasing the temperature will also enhance the EMSI effect due to slower through-plane lithium-ion transport. The depth of discharge, or more precisely the SOC window in which the cell is cycled, is also relevant, as the EMSI effect will occur only if the cell is cycled in an SOC-range in which the active material volume is changing, e.g., cycling the cell between SOCs of 40 and 70% (see Figure 1c and d) should suppress electrolyte motion and therefore also the EMSI effect. This matches the observation by Morales Torricos et al.[14] that cycling between 40-60% SOC effectively suppresses the capacity loss (and subsequent capacity recovery, see below) in 18650 NCA/silicon-graphite cells. Lastly, rest times in the cycling procedure will reduce the EMSI effect, but to properly assess this, we first need to consider space and time in lithium-ion battery cells.

Accelerated ageing tests versus real cell applications.- For cells in which no electrolyte motion takes place on a cm-scale, the only relevant dimension on which lithium concentration gradients occur is the through-plane dimension, either within the active material particles (≈ 1 to ≈ 10 µm) or in the liquid electrolyte (≈ 100 to ≈ 200 µm); considering typical solid and liquid lithium diffusion coefficients ($\approx 1 \cdot 10^{-10}$ cm^2/s for solid diffusion, $\approx 1 \cdot 10^{-6}$ cm^2/s for liquid diffusion),[40,56] these through-plane concentration gradients equilibrate on the time scales of minutes to hours (see Figure 9c). This is the same time scale on which cycles in a typical accelerated aging test take place (e.g., ≈ 4 hours for C/2/C/2 cycling), meaning that every cycle is a perfect repetition of the previous one if one neglects irreversible aging, which takes place over hundreds of cycles. In contrast, the in-plane concentration gradient created by the EMSI effect occurs on a cm-scale (depending on cell dimensions) and therefore takes weeks to months to equilibrate. This has important implications for the design and interpretation of accelerated ageing tests, as the cell properties change gradually from cycle to cycle: A straightforward interpretation of Figure 4a and b would be that the low electrolyte cell can withstand the fast charge profile while the high electrolyte cells cannot. In reality, the through-plane lithium-ion transport is equally good (or better) in the high electrolyte cell and fast enough to sustain the fast charge profile, but only until the

emerging in-plane concentration gradient starts to have a significant adverse effect. Therefore, an alternative interpretation of Figure 4 would be that the high electrolyte cell can indeed sustain the fast-charging protocol, but only for a limited number of consecutive cycles without rest (≈ 20, as indicated by the onset of discharge endpoint slippage and average discharge voltage), which might however be sufficient for a commercial application. One way to alleviate this is to reduce charge-throughput in Ah/days by introducing rest periods and giving time for the in-plane concentration gradient to relax; however, due to the long equilibration distance, this requires weeks to months rather than minutes or hours. Therefore, the EMSI effect introduces a fundamental conflict between fast testing times and relevant testing data. Essentially, the in-plane $LiPF_6$ concentration gradient acts as a "long-term memory" for lithium-ions cells in the sense that the cycling history of the previous weeks or months will affect the state of the cell and its response to further testing.

Capacity & resistance recovery.- As mentioned in the introduction, a "capacity recovery effect" has been reported when cycling large format cells at high C-rates.[12–15] To check whether the capacity recovery effect would also occur in our 4695 cells and might be linked to the EMSI effect, we additionally subjected two high and two low electrolyte cells to 48 cycles of fast-charging (i.e., 8 repetitions of the 3x C/2/C/2 + 3x fast charge/C/2 sequence), which resulted in ≈ 6% capacity loss for the high electrolyte and ≈ 1% capacity loss for the low electrolyte cells (Figure 9d, left panel). After cycling, these cells rested for 50 days at 0% SOC and then underwent a second RPT, in which the capacity of the high electrolyte cells increased from 94% (red solid bars) back to 98% (red dashed bars), while the low electrolyte cells almost approached their original capacity (filled and dashed blue bars). In addition to this capacity recovery, the cells also exhibited a resistance recovery (Figure 9d, right panel). During the 50 days rest period, the DCIR of the high electrolyte cells decreased from 120% (red filled bar) back to 101% (red dashed bar), whereas the DCIR of the low electrolyte cells decreased from 101% directly after cycling to 97% after storage. In short, the initial aging (6% capacity loss, 20% DCIR increase) of the high electrolyte cells is largely reversible on a time scale of weeks, meaning that at least up to 48 cycles, irreversible lithium plating is only partially responsible for the observed cell deterioration. Rather, the EMSI effect itself might lead to an apparent capacity loss and resistance increase, which both subside as the in-plane $LiPF_6$ gradient levels out during the storage period.

The resistance recovery is probably a direct consequence of the EMSI effect as the redistribution of $LiPF_6$ causes a deviation from the electrolyte conductivity optimum at 1.0 – 1.2 mol/L.[40] While a quantitative analysis of the influence of the in-plane salt gradient on DCIR is beyond the scope of this manuscript, a resistance increase of 20% is on the right order of magnitude for a change in $LiPF_6$ concentration (compare Table VI and related discussion in ref. [57]).

The capacity recovery might also be a consequence of the EMSI effect due to increased local electrolyte resistance; eventually, areas with a $LiPF_6$ concentration below (or above) a certain threshold might not fully contribute to the cell capacity anymore, causing an "apparent" capacity loss. As the in-plane $LiPF_6$ gradient equilibrates upon prolonged storage, these areas can fully be lithiated again, leading to an

apparent gain in capacity. If, in contrast, the cells do not rest but continue cycling, secondary side reactions such as lithium plating can occur in the areas with high/low $LiPF_6$ concentrations, especially when charging at high C-rates, which then causes irreversible cell aging.

The mechanistic connection of EMSI effect and capacity/resistance recovery, as suggested above, is supported by the fact that the recovery effect has been only reported for cylindrical cells i) with high electrolyte amounts (see Figure 1 in ref. [15]) and ii) if the cycling occurs in a SOC window with active material volume change.[14] Nevertheless, other or additional origins of the capacity/resistance recovery are also possible (e.g. inhomogeneous distribution of active lithium[13,14]) and further research is necessary to obtain a complete understanding of the mechanisms and conditions under which recovery effects can appear in lithium-ion cells.

Conclusion

In this study, we have demonstrated that the combination of electrolyte motion and the through-plane $LiPF_6$ concentration gradient occurring at high charging C-rates causes the development of a severe in-plane $LiPF_6$ concentration gradient along the jelly roll axis in 4695 cylindrical cells, leading to a deviation in $LiPF_6$ concentration at the edges and the center of more than ± 50% in comparison to the initial average concentration after only 18 fast charge cycles. This in-plane $LiPF_6$ concentration gradient has a severe impact on cell resistance and capacity and eventually causes highly localized lithium plating. We call this effect *electrolyte motion induced salt inhomogeneity* (EMSI) and consider it of high significance not only for cylindrical cells but any large-format lithium-ion cell under high compression, as it likely governs the lifetime of these cells during long-term fast-charge cycling.

We also propose a mechanism for how electrolyte motion causes an in-plane $LiPF_6$ gradient with different in-plane permeabilities of anode and cathode for electrolyte flow as the root cause. For the cells employed in this study, the conducting salt was enriched in the jelly-roll center and depleted at the jelly-roll edges, but the gradient might also be reversed for other electrode designs. As the in-plane concentration gradient is reversible on the timescale of several weeks, the EMSI effect is a possible explanation of the "capacity recovery effect" which has previously been described by other groups. Furthermore, we demonstrate that reducing the electrolyte amount to a pore filling ratio of < 1 at 100% SOC can effectively eliminate electrolyte motion and therefore also suppresses the development of the in-plane concentration gradient, which is the likely (reverse) explanation for the recently reported "high volume effect".

Methods

Estimation of the pore filling ratio

Unit cell volume expansion. – The unit cell volume expansion for graphite was digitalized and fitted from Figure 5c in ref.[25]. For NMC, the Figure S6 in ref.[29] was digitalized and the x-axis converted from potential into state-of lithiation (SOL); the nickel content in the cited study is slightly lower than in the active material used in our study but this does not significantly affect the volume estimation. For silicon, volume expansion is calculated based on the constant volume requirement of 8.9 mL per mol of lithium.[26]

SOL-SOC correlation. - The SOL as a function of cell SOC for the different active materials was determined based on their respective half-cell open-circuit voltage (OCV) curves and a differential voltage analysis of the full-cell OCV curves (see Figure 1a in ref.[54] for an example). The SOL values in Figure 1b are based on the discharge (= delithiation of anode active material) OCV curves. The SOL vs. SOC correlation of graphite and silicon differs slightly during charging and discharging due to the silicon voltage hysteresis (see Figure 1b in ref.[54] and Figure 2c in ref.[53]). Therefore, also the active material volume exhibits a slight hysteresis, but we refrained from repeating the same analysis for the charging OCV curve as it does not offer significant additional information but increases the complexity.

SOL definitions for silicon. - In Figure 1a, the SOL of silicon is defined as x in $L_{3.75x}Si$ which corresponds to the theoretical specific capacity $Q_{theo.}(Si)$ of 3590 mAh/g. Unlike for graphite and NMC, the practically achievable specific capacity of silicon $Q_{real}(Si)$ is significantly lower, a typical ratio of $Q_{real}(Si)/Q_{theo.}(Si)$ falls in the range of 30 - 70% when used in a graphite-composite electrode. Therefore, in Figure 2b the SOL for silicon refers to $Q_{real}(Si)$, not $Q_{theo.}(Si)$. These details of silicon SOL definition do not affect the volume calculation though, as – fortunately – silicon expands by 8.9 mL per mol of lithium irrespective of the actual SOL.

Material densities. - For the different materials we used density values provided by material suppliers and literature. Partially, we also measured material densities using He-pycnometer as will be explained in detail in a follow-up publication.

Computer tomography and jelly roll volume. – Computer tomography (CT) scans were conducted at 25 °C at 100% SOC (CCCV charge to 4.2 V, C/3 with C/50 cut-off) and at 0% SOC (CC discharge to 2.8 V, C/3). CT scans were recorded with a Phoenix V|tome|x M (Waygate Technologies) with 250 kV voltage, 260 µA cathode current, 2000 images per scan and 32 µm voxel size. After image reconstruction, the outer and inner jelly roll diameter were determined from cross-section images taken at several positions along the height of the jelly roll to calculate the jelly roll volume.

Moment of inertia measurement

Moment of inertia measurements were carried out on the commercially available system Resonic T (Resonic GmbH, Berlin, Germany) which is displayed in Figure S1. The measurements were not carried out in *operando*-mode, but at pre-set SOCs without cables attached to the cell. To set the desired SOC (0 or 100% SOC), cells were charged or discharged at a C/15 rate to 2.8 or 4.2V, followed by a CV phase with a C/20 current cut-off. The cells were then rapidly transferred onto an air-bearing pendulum, fixed in a horizontal position and the moment of inertia measurements were performed. Independent impulses were used to drive the oscillation of the cell-pendulum setup. For each impulse, the oscillation frequency f was derived from a movement sensor signal, using 10 oscillation cycles. This was repeated 10 times and the averaged f value was used to obtain a single measurement for the moment of inertia I of the cell using the relation $f = (1/2\pi) * \sqrt{(k/I)}$, where k is the spring constant of $k = 0.3082$ Nm. To ensure accuracy, the moment of inertia measurement was repeated three times, taking approximately 4

minutes (for 30 independent impulses). The evolution of the moment of inertia was monitored for 45 minutes after the end of (dis)charging, in intervals of 15 minutes.

This spring constant and the typical moment of inertia of a 4695 cell result in a quite low oscillation frequency of ≈ 3 Hz which is advantageous as 1) it prevents affecting the electrolyte distribution inside the cell (no "centrifugation" of electrolyte) and 2) it reduces the influence of mechanical elasticity of the cells on the moment of inertia measurements.

Cell cycling

Table 2 Cycling protocol, consisting of reference performance tests (RPT, steps 1-26) at 25 °C and aging cycling (steps 27-38) at 35 °C.

		Nr	Step
Reference performance test (RPT, T = 25 °C)	Capacity Check	1	CC discharge with C/3 to 2.8 V
		2	Rest ~15 min
		3	CCCV charge with C/3 to 4.2 V and I < C/50
		4	Rest ~15 min
		5	CC discharge with C/3 to 2.8 V
		6	Rest ~15 min
		7	Repeat steps 1-6 3x (= 3 cycles, 3rd discharge is used as RPT capacity)
	DCIR	8	CCCV charge with C/3 to 4.2 V and I < C/50
		9	Rest ~15 min
		10	CC discharge with C/3 to 80% SOC
		11	Rest ~1 h
		12	CC discharge with 2 C for 30 s
		13	Rest ~15 min
		14	CC discharge with C/3 to 50% SOC
		15	Rest ~1 h
		16	CC discharge with 2 C for 30 s
		17	Rest ~15 min
		18	CC discharge with C/3 to 20% SOC
		19	Rest ~1 h
		20	CC discharge with 2 C for 30 s
		21	Rest ~15 min
		22	CC discharge with C/3 to 2.8 V
	Only BOL RPT	23	Rest ~15 min
		24	CCCV charge with C/3 to 4.2 V and I < C/50
		25	Rest ~15 min
		26	CC discharge with C/20 to 2.8 V (Determine $U_{10\%}$)
Cycling (T = 35 °C)	3x C/2/C/2	27	CCCV charge with C/2 to 4.2 V and I < C/50
		28	Rest ~ 15 min
		29	CCCV discharge with C/2 to $U_{10\%}$ and I < C/50
		30	Rest ~ 15 min
		31	Repeat steps 27-30 3x (= 3 cycles)
	3x FC/C/2	32	FC cycling: charge with FC profile to 80% SOC C/2 cycling: CC charge with C/2 to 80% SOC
		33	Rest ~ 15 min
		34	CCCV discharge with C/2 to $U_{10\%}$ and I < C/50
		35	Rest ~ 15 min
		36	Repeat steps 32-35 3x (= 3 cycles)
		37	Rest ~ 3 h
		38	Repeat steps 27-37 8x (= 48 cycles)
		39	Repeat steps 1-38 until 130 cycles

The cycling protocol is given in detail in Table 2. Reference performance tests (RPTs) were performed at 25 °C at begin of life (BOL) and after every 48th cycle (6 sequences of 3 C/2/C/2 + 3 fast charge/C/2 cycles, see below). The RPT consisted of 3 charge/discharge cycles from 0-100% SOC with a C/3 CCCV charge/C/3 CC discharge (steps 1-7 in Table 2) followed by a 30 s 2C discharge pulse test at 80%, 50% and 20% SOC (steps 8-22). For the RPT at BOL, a C/20 discharge curve was measured after the discharge pulse test to determine the voltage $U_{10\%}$ corresponding to 10% SOC (see steps 23-26).

After initial RPT, temperature was changed to 35 °C and cells were cycled in a repeating sequence of 3 cycles from 10-100% SOC with C/2 CCCV charge/C/2 CCCV discharge (steps 27-31), followed by 3 cycles from 10-80% SOC with a multi-step constant current (MSCC) fast charge profile/C/2 CCCV discharge (steps 32-36). The rest time between all each charge and discharge steps was set to a constant time corresponding to ~15 min (exact time cannot be disclosed). The fast charge profile was selected to achieve a charging time of 16-21 min while avoiding lithium plating at higher SOCs (for details see Figure S3). During cycling, the fast charge profile was adapted to the actual cell capacity according to $I_{FC} = C_{FC}*Q_{100\%-10\%}/0.9$, with I_{FC} being the adapted fast charge current applied to the cell, C_{FC} the C-rate of the current fast charge step, and $Q_{100\%-10\%}$ the capacity from the most recent 100%-10% C/2 discharge. After the 3 fast charge cycles, the cells rested for ~3 h at 10% SOC before the sequence began anew (steps 37-38). For the fast charge procedure, two different vertical orientations were tested, namely the positive terminal facing upwards or downwards. Reference cells were cycled with an identical sequence with the positive terminal facing up, but the fast charge profile was replaced with a C/2 charge from 10-80% SOC.

Cell cycling and RPTs were performed on an HRT-L-150A high resolution battery tester current precision < 1.5 mA, voltage precision < 4 µV, both based on typical RMS noise; Battery Dynamics GmbH, Germany) in a temperature chamber (LabEvent T/500/30/3, temporal temperature deviation ± 0.5 K, spatial temperature homogeneity ± 2 K; Weiss Technik GmbH, Germany) at Battery Dynamics GmbH, Germany. All test conditions were performed with two nominally identical cells. In the results section, the average of each cell pair is given, as well as their min/max value as error bars.

Determination of $LiPF_6$ concentration and α(EC)

Electrolyte extraction. - Cells were discharged to 2.8 V and an additional CV phase with a current cut-off of C/50 was applied to ensure full discharge. After discharge, cells were allowed to rest for 24 to 48 hours before cell opening to ensure the relaxation of any local $LiPF_6$ through-plane concentration gradient between anode and cathode as already explained above. This is important as we are interested in long scale (cm-scale, typical relaxation time weeks to months) concentration gradients within the electrode, not the well-known anode/cathode (µm-scale, typical relaxation time minutes to hours) concentration gradients. After the rest period, cells were opened inside an argon-filled glove box (O_2 < 0.1 ppm, H_2O < 1 ppm, MBraun, Germany) and the jelly rolls were extracted. The jelly roll was unrolled to roughly 50% of its length of ≈ 5 m and anode and cathodes were immediately separated from the adhering separators. We found that leaving the separators stick to the electrodes slightly reduced the recovered $LiPF_6$ amounts, probably because electrolyte is partially sucked into the separator during evaporation and drags along the dissolved $LiPF_6$. Electrode coins were punched out at different positions along the z-axis (jelly roll height) as displayed in Figure S4. For ion-chromatography (IC), electrode coins with a diameter of 12.7 mm were punched out very close to the edges of the electrode (≈ 1 mm from coating edge) and in the center of the electrode using a precision puncher (Hohsen, Japan). 15 coins were punched in each z-axis position (see Figure S4), united in one glass vial each and 5 mL of an extraction solvent added. For liquid chromatography-mass spectrometry (LC-MS) coins with a diameter of 20 mm were punched out at distance of ≈ 3 mm to the electrode edges and in the electrode center using a precision puncher (Hohsen, Japan). Two coins were punched in each z-axis position, placed in individual plastic tubes and 2.5 mL of an extraction solvent was added. Therefore, for each z-axis position we obtain one IC sample and two independent LC-MS samples. Acetonitrile (anhydrous, >99.8%, Sigma Aldrich, United States) was used as extraction solvent for cathode coins and dimethyl

carbonate (extra dry 99+% Acro Seal™, Thermo Scientific GmbH, Germany) for anode coins. After addition of the extraction solvent, the plastic tubes were placed on a shaker plate inside the glove box for at least 16 hours before performing IC and LC-MS analysis.

IC and LC-MS analysis. - The concentrations of Li^+ and PF_6^- in the extraction solvent were determined by IC using a Metrohm 850 Professional IC (Metrohm, Germany) equipped with an ionic conductivity sensor. Details on the procedure can be found in our previous publication.[57] As mentioned above, Li^+ and PF_6^- concentrations were identical within ± 5% for all sample and therefore averaged into a single $LiFP_6$ concentration. Only for samples with a very low concentration corresponding to less than 0.1 mol/L_{pore} in Figure 6, for unknown reasons Li^+/PF_6^- ratios were increased up to ≈1.4 but this is irrelevant for the further interpretation. For quantification of ethylene carbonate (EC) and PF_6^-, the samples were separated by means of an Vanquish™ Core Binary LC (Thermo Fisher Scientific GmbH, Dreieich, Germany) consisting of Vanquish binary pump, an Vanquish autosampler, a Vanquish column compartment and a Vanquish Diode array detector. The chromatographic system was connected to a Orbitrap Exploris 120 (Thermo Fisher Scientific GmbH, Dreieich, Germany) controlled by the Thermo Scientific Xcalibur software (version 4.6). Detection was achieved using an electrospray ionization source (H-ESI). Data interpretation was performed using Thermo Scientific™ TraceFinder™ software (version 5.1). The samples were separated by a Raptor™ FluoroPhenyl column (2.7 µm, 150 × 2.1 mm; Thames Restek, UK Ltd.). A gradient of formic acid (0.02%) in water/acetonitrile (98/2; v/v) (solvent A) and formic acid (0.02%) in acetonitrile/water (95/5; v/v) (solvent B) at a flow of 0.4 mL/min was used for the separation: 0-1 min 0% B; 10-13 min 100% B, 14-17 min 0% B. Solvents used for LC-MS analysis were of hypergrade LC-MS grade (Merck, Darmstadt, Germany). Water for chromatography was purified using a Milli-Q IQ 7000 system (Merck, Darmstadt, Germany). Detection was operated in the tMS^2 H-ESI mode (ion spray voltage: 2000 V) using the following instrument settings: sheath gas (50 Arb), aux gas (10 Arb), ion transfer tube temperature (325°C) and Vaporizer Tem (325°C). For the quantification of EC and PF_6^- external calibration was performed. While we recorded daily EC calibration curves, we missed to also do so for PF_6^- for the 130 cycle cells. Due to day to day variation of the calibration curves, we could therefore not quantify the PF_6^- amounts in units of mol which is the reason why Figure 6c,d,e,h,i and j miss the two second-outermost $LiPF_6$ data points which are only sampled by LC-MS (see Supporting Information for further details). A relative comparison (normalized to the respective center positions) is displayed in Figure S6. As shown by IC, Li^+ and PF_6^- concentrations agreed within ± 5% and therefore the PF_6^- concentration determined by LC-MS was treated as equivalent to a $LiPF_6$ concentration.

Calculation of $c(LiPF_6)_{Pore}$ and $\alpha(EC)$. - The calculation of $c(LiPF_6)_{Pore}$ and $\alpha(EC)$ as displayed in Figure 6 also requires the respective pore volumes of anode and cathode coins from which the $LiPF_6$ and EC were extracted. For this, pore volumes of pristine anodes and cathodes were used which can easily be calculated based on electrode loading (in mg/cm^2), electrode composition, material densities and coating thickness after calendaring. While this is the standard procedure used in literature,[23] this pristine electrode pore volume differs in two ways from the "real" pore volume after formations: i) the anode porosity is reduced due to SEI build-up and ii) the jelly-roll (or electrode stack) expands during cell formation which increases the pore volume (volume which is initially "outside" of the jelly-roll turns into pore volume). In the calculation of the total pore volume (aggregate of anode, cathode, and separator porosity) which is displayed in Figure 1c, both effects are included: the SEI volume is approximated by the FEC reduction model, and the jelly roll expansion is incorporated as the actual jelly roll volume after formation is determined by CT-scans. Unfortunately, it is very challenging to precisely determine individual anode and cathode coating layer thicknesses in a 4695 cell from laboratory CT-scans and therefore it is not possible to assign the pore volume gained by jelly-roll expansion to anode and cathode. Therefore, pristine electrode pore volumes were used for the calculation of $c(LiPF_6)_{Pore}$ and $\alpha(EC)$ as displayed in Figure 6.

The good match between $c(LiPF_6)_{Pore}$ and $\alpha(EC)$ values with the expected values as observed for the high electrolyte BOL cells (Figure 6a) justifies using pristine electrode pore volumes. Nevertheless,

caution is required with respect to the absolute $c(LiPF_6)_{Pore}$ concentrations displayed in Figure 6 as they rely on the use of electrode porosity as a rather "poorly calibrated pipette"; in contrast, the relative $LiPF_6$ concentration profiles are more robust as any error in the assumed pore volume would only cause a systematic parallel shift of all concentration profiles displayed in Figure 6.

Simulations

Simulations were conducted using the Abaqus software (Dassault Systèmes) and a two-dimensional finite element mesh to perform a fully coupled analysis of thermal, electrochemical, structural, and pore pressure effects. In through-plane direction, the model geometry consists of a single stack of anode, separator, and cathode. In in-plane direction, the model includes half the jelly roll height, assuming a symmetry plane at the center of the jelly roll. Additionally, an expandable donut volume, which can uptake free electrolyte, is appended at the edge of the jelly roll. The simulations are based on the Doyle-Fuller-Newman (DFN) approach[41,42] coupled with an electrolyte pore flow model and a 0D lumped thermal model. All DFN input parameters, including geometric, electrochemical, and thermal properties, were obtained from a fully validated model of a high-energy lithium-ion battery by O'Regan et al.[58] Based on this model, a few adjustments were made, which are described in the following. It was assumed that the anode particles undergo a total volume expansion of 13% during intercalation from state of lithiation 0 to 100%. To model rigid clamping, all nodes of the finite element mesh belonging to the jelly roll were fixed in position, while the donut volume was allowed to expand/contract in the in-plane direction. Consequently, the volume changes in the particles result in a reduction in porosity, causing the expulsion of electrolyte from the jelly roll into the donut volume. Since the original model by O'Regan does not include porosity reduction due to swelling, the Bruggeman coefficient in the anode coating was adjusted to a value of 1.37 to still match the experimentally measured cell voltage. Furthermore, it was discovered that the extraordinary low values for solid diffusivity reported by O'Regan led to numerical instabilities. Therefore, these values were adjusted to values found for similar materials by Sturm et al.[56] These are 5e-14 m^2/s for anode particles and 5e-13 m^2/s for cathode particles. For the electrolyte pore flow model, the saturation of electrolyte in the pores was maintained at a constant value of 100% throughout the simulation. Furthermore, the permeability values were adjusted to be three times higher in the anode coating compared to the cathode and separator regions.

Conflict of interest

There are no conflicts to declare.

Acknowledgment

We thank Daniel Pritzl, Niclas Emrich, Adele Birrozzi, Fabienne Biggoer and Frank Kiesewetter (all BMW Group) for their support in cell assembly, analysis, and electrochemical simulations. We also thank Benjamin Strehle and Peter Keil (Battery Dynamics GmbH, Garching, Germany) for support with cell cycling and data analysis. Finally, we want to acknowledge Robert Klöpper and Oliver Kolakowski (Resonic GmbH, Berlin, Germany) for helpful advice with the moment of inertia measurements.

CRediT Authorship

Sophie Solchenbach – Conceptualization, Investigation, Data curation, Writing – original draft, Camilla Tacconis – Investigation, Methodology, Aurora Gomez Martin – Investigation, Supervision, Verena Peters – Investigation, Data curation, Lea Wallisch – Investigation, Anna Stanke – Investigation, Johanna Hofer – Investigation, Diemo Renz – Investigation, Visualization, Burkhard Lewerich – Methodology, Georg Bauer – Methodology, Moritz Wichmann – Investigation, Daniel Goldbach – Investigation, Alexander Adam, – Investigation, Markus Spielbauer – Investigation, Peter Lamp – Resources, Johannes Wandt – Conceptualization, Investigation, Data curation, Writing – original draft

References

1 J. T. Frith, M. J. Lacey and U. Ulissi, *Nature communications*, 2023, **14**, 420.
2 K. G. Gallagher, S. E. Trask, C. Bauer, T. Woehrle, S. F. Lux, M. Tschech, P. Lamp, B. J. Polzin, S. Ha, B. Long, Q. Wu, W. Lu, D. W. Dees and A. N. Jansen, *J. Electrochem. Soc.*, 2016, **163**, A138-A149.
3 Y. Qiu, X. Zhang, C. Usubelli, D. Mayer, C. Linder and J. Christensen, *Journal of Power Sources*, 2022, **541**, 231632.
4 Y. Xie, S. Wang, R. Li, D. Ren, M. Yi, C. Xu, X. Han, L. Lu, B. Friess, G. Offer and M. Ouyang, *Journal of Power Sources*, 2022, **542**, 231753.
5 A. J. Smith, Y. Fang, A. Mikheenkova, H. Ekström, P. Svens, I. Ahmed, M. J. Lacey, G. Lindbergh, I. Furó and R. W. Lindström, *Journal of Power Sources*, 2023, **573**, 233118.
6 T. C. Bach, S. F. Schuster, E. Fleder, J. Müller, M. J. Brand, H. Lorrmann, A. Jossen and G. Sextl, *Journal of Energy Storage*, 2016, **5**, 212–223.
7 D. Petz, V. Baran, J. Park, A. Schökel, A. Kriele, J. Rebelo Kornmeier, C. Paulmann, M. Koch, T. Nilges, P. Müller-Buschbaum and A. Senyshyn, *Batteries*, 2024, **10**, 68.
8 A.-S. Hamedi, F. Pouraghajan, F. Sun, M. Nikpour and D. R. Wheeler, *J. Electrochem. Soc.*, 2022, **169**, 20551.
9 F. B. Spingler, S. Friedrich, S. Kücher, S. Schmid, D. López-Cruz and A. Jossen, *J. Electrochem. Soc.*, 2021, **168**, 110515.
10 C. Fear, M. Parmananda, V. Kabra, R. Carter, C. T. Love and P. P. Mukherjee, *Energy Storage Materials*, 2021, **35**, 500–511.
11 M. M. Forouzan, B. A. Mazzeo and D. R. Wheeler, *J. Electrochem. Soc.*, 2018, **165**, A2127-A2144.
12 J. Keil, N. Paul, V. Baran, P. Keil, R. Gilles and A. Jossen, *J. Electrochem. Soc.*, 2019, **166**, A3908-A3917.
13 M. Lewerenz, P. Dechent and D. U. Sauer, *Journal of Energy Storage*, 2019, **21**, 680–690.
14 P. Morales Torricos, C. Endisch and M. Lewerenz, *Batteries*, 2023, **9**, 230.
15 A. Bonakdarpour, I. Stoševski, A. Tiwari, S. R. Smith, B. M. Way and D. P. Wilkinson, *J. Electrochem. Soc.*, 2024, **171**, 20543.
16 B. Gyenes, D. A. Stevens, V. L. Chevrier and J. R. Dahn, *J. Electrochem. Soc.*, 2015, **162**, A278-A283.
17 Y. Hao, K. Li, S. Zhang, J. Wang, X. Zhu, W. Meng, J. Qiu and H. Ming, *ACS applied materials & interfaces*, 2024, **16**, 27400–27409.
18 M. Lanz, E. Lehmann, R. Imhof, I. Exnar and P. Novák, *Journal of Power Sources*, 2001, **101**, 177–181.
19 M. J. Mühlbauer, O. Dolotko, M. Hofmann, H. Ehrenberg and A. Senyshyn, *Journal of Power Sources*, 2017, **348**, 145–149.
20 N. S. Nazer, M. Strobl, A. Kaestner, P. J. S. Vie and V. A. Yartys, *Electrochimica Acta*, 2022, **427**, 140793.
21 C. P. Aiken, N. Kowalski, R. C. Fitzner, S. Trussler, J. E. Harlow, E. J. Butler and J. R. Dahn, *J. Electrochem. Soc.*, 2023, **170**, 40529.
22 M. Ank, A. Sommer, K. Abo Gamra, J. Schöberl, M. Leeb, J. Schachtl, N. Streidel, S. Stock, M. Schreiber, P. Bilfinger, C. Allgäuer, P. Rosner, J. Hagemeister, M. Rößle, R. Daub and M. Lienkamp, *J. Electrochem. Soc.*, 2023, **170**, 120536.
23 F. J. Günter, C. Burgstaller, F. Konwitschny and G. Reinhart, *J. Electrochem. Soc.*, 2019, **166**, A1709.
24 S. J. An, J. Li, D. Mohanty, C. Daniel, B. J. Polzin, J. R. Croy, S. E. Trask and D. L. Wood, *J. Electrochem. Soc.*, 2017, **164**, A1195-A1202.

25 S. Schweidler, L. de Biasi, A. Schiele, P. Hartmann, T. Brezesinski and J. Janek, *J. Phys. Chem. C*, 2018, **122**, 8829–8835.
26 M. N. Obrovac and V. L. Chevrier, *Chemical reviews*, 2014, **114**, 11444–11502.
27 L. Y. Beaulieu, T. D. Hatchard, A. Bonakdarpour, M. D. Fleischauer and J. R. Dahn, *J. Electrochem. Soc.*, 2003, **150**, A1457.
28 L. de Biasi, A. O. Kondrakov, H. Geßwein, T. Brezesinski, P. Hartmann and J. Janek, *J. Phys. Chem. C*, 2017, **121**, 26163–26171.
29 F. Friedrich, B. Strehle, A. T. S. Freiberg, K. Kleiner, S. J. Day, C. Erk, M. Piana and H. A. Gasteiger, *J. Electrochem. Soc.*, 2019, **166**, A3760-A3774.
30 M. Wetjen, D. Pritzl, R. Jung, S. Solchenbach, R. Ghadimi and H. A. Gasteiger, *J. Electrochem. Soc.*, 2017, **164**, A2840-A2852.
31 C. Berg, R. Morasch, M. Graf and H. A. Gasteiger, *J. Electrochem. Soc.*, 2023, **170**, 30534.
32 F. J. Günter, J. B. Habedank, D. Schreiner, T. Neuwirth, R. Gilles and G. Reinhart, *J. Electrochem. Soc.*, 2018, **165**, A3249-A3256.
33 R. Morasch, J. Keilhofer, H. A. Gasteiger and B. Suthar, *J. Electrochem. Soc.*, 2021, **168**, 80519.
34 A. J. Smith, J. C. Burns, D. Xiong and J. R. Dahn, *J. Electrochem. Soc.*, 2011, **158**, A1136-A1142.
35 M. Ulldemolins, F. Le Cras and B. Pecquenard, *Electrochemistry Communications*, 2013, **27**, 22–25.
36 S. Wen, B. Lu, Y. Zhao, Y. Song and J. Zhang, *Journal of Power Sources*, 2021, **495**, 229763.
37 F. Grimsmann, T. Gerbert, F. Brauchle, A. Gruhle, J. Parisi and M. Knipper, *Journal of Energy Storage*, 2018, **15**, 17–22.
38 T. Roth, A. Frank, F. Oehler, A. Graule, S. Kücher and A. Jossen, *J. Electrochem. Soc.*, 2024, **171**, 50547.
39 L. O. Valøen and J. N. Reimers, *J. Electrochem. Soc.*, 2005, **152**, A882.
40 J. Landesfeind and H. A. Gasteiger, *J. Electrochem. Soc.*, 2019, **166**, A3079-A3097.
41 M. Doyle, T. F. Fuller and J. Newman, *J. Electrochem. Soc.*, 1993, **140**, 1526–1533.
42 T. F. Fuller, M. Doyle and J. Newman, *J. Electrochem. Soc.*, 1994, **141**, 1–10.
43 R. Morasch, H. A. Gasteiger and B. Suthar, *J. Electrochem. Soc.*, 2023, **170**, 80522.
44 R. Koerver, W. Zhang, L. de Biasi, S. Schweidler, A. O. Kondrakov, S. Kolling, T. Brezesinski, P. Hartmann, W. G. Zeier and J. Janek, *Energy Environ. Sci.*, 2018, **11**, 2142–2158.
45 A. Davoodabadi, J. Li, H. Zhou, D. L. Wood, T. J. Singler and C. Jin, *Journal of Energy Storage*, 2019, **26**, 101034.
46 J. B. Habedank, F. J. Günter, N. Billot, R. Gilles, T. Neuwirth, G. Reinhart and M. F. Zaeh, *Int J Adv Manuf Technol*, 2019, **102**, 2769–2778.
47 M. P. Lautenschlaeger, B. Prifling, B. Kellers, J. Weinmiller, T. Danner, V. Schmidt and A. Latz, *Batteries & Supercaps*, 2022, **5**.
48 B. Suthar, J. Landesfeind, A. Eldiven and H. A. Gasteiger, *J. Electrochem. Soc.*, 2018, **165**, A2008-A2018.
49 Z. Deng, Z. Huang, Y. Shen, Y. Huang, H. Ding, A. Luscombe, M. Johnson, J. E. Harlow, R. Gauthier and J. R. Dahn, *Joule*, 2020, **4**, 2017–2029.
50 P. M. Attia, A. Bills, F. Brosa Planella, P. Dechent, G. dos Reis, M. Dubarry, P. Gasper, R. Gilchrist, S. Greenbank, D. Howey, O. Liu, E. Khoo, Y. Preger, A. Soni, S. Sripad, A. G. Stefanopoulou and V. Sulzer, *J. Electrochem. Soc.*, 2022, **169**, 60517.
51 C. Kupper, B. Weißhar, S. Rißmann and W. G. Bessler, *J. Electrochem. Soc.*, 2018, **165**, A3468-A3480.
52 A. A. Wang, S. Greenbank, G. Li, D. A. Howey and C. W. Monroe, *Cell Reports Physical Science*, 2022, **3**, 101047.
53 H. Pegel, O. von Kessel, P. Heugel, T. Deich, J. Tübke, K. P. Birke and D. U. Sauer, *Journal of Power Sources*, 2022, **537**, 231443.
54 D. Vidal, C. Leys, B. Mathieu, N. Guillet, V. Vidal, D. Borschneck, P. Chaurand, S. Genies, E. de Vito, M. Tulodziecki and W. Porcher, *Journal of Power Sources*, 2021, **514**, 230552.

55 J. R. Dahn, Watching Electrolyte Move in Cylindrical Li-ion Cells and Why This Matters, International Battery Seminar, Orlando, 2024.
56 J. Sturm, A. Rheinfeld, I. Zilberman, F. B. Spingler, S. Kosch, F. Frie and A. Jossen, *Journal of Power Sources*, 2019, **412**, 204–223.
57 L. Hartmann, L. Reuter, L. Wallisch, A. Beiersdorfer, A. Adam, D. Goldbach, T. Teufl, P. Lamp, H. Gasteiger and J. Wandt, *J. Electrochem. Soc.*, 2024.
58 K. O'Regan, F. Brosa Planella, W. D. Widanage and E. Kendrick, *Electrochimica Acta*, 2022, **425**, 140700.